1-1-2011

Corrosion behaviour of nanocomposite TiSiN coatings on steel substrates

Mohammad Ahmed
Edith Cowan University

Paul Munroe

Zhong-Tao Jiang

Xiaoli Zhao
Edith Cowan University

William Rickard

See next page for additional authors

10.1016/j.corsci.2011.07.011

Elsevier Editorial System(tm) for Corrosion Science
Manuscript Draft

Manuscript Number:

Title: Corrosion behaviour of nanocomposite TiSiN coatings on steel substrates

Article Type: Full Length Article

Keywords: A. Nanocomposite coatings; B.Corrosion; C. Residual stress; c.Focused ion beam microscopy; d. Finite element analysis; e. Surface defects

Corresponding Author: Mr. Mohammad Shoeb Ahmed,

Corresponding Author's Institution: Edith Cowan University

First Author: Mohammad Shoeb Ahmed

Order of Authors: Mohammad Shoeb Ahmed; Paul Munroe; Zhong-Tao Jiang; Xiaoli Zhao; William Rickard; Zhi-feng Zhou; Lawrence K Y Li; Zonghan Xie

Abstract: Nanocomposite TiSiN coatings were deposited on tool steels. Detailed mechanisms that govern the corrosion of these coated steels were revealed, following immersion tests in 70% nitric acid solution. Pitting occurred preferentially at surface defect sites and expanded with increasing immersion time. Both Young's modulus and hardness decreased as the corrosion damage intensified. A thin oxide layer formed during thermal annealing at 900°C was found to be effective against corrosive attack. In addition, compressive residual stress was noted to suppress the propagation of corrosion-induced cracks. Role of residual stress in controlling the corrosion resistance of these ceramic-coated steels was clarified.

Dear Editor,

Ceramic nanocomposite coatings offer great potential for surface engineering of metal components used for cutting tools and medical devices. However, a deeper understanding of the roles of coating microstructure and residual stress in corrosion prevention remains lacking. In this work, an array of surface and subsurface characterisation techniques including focused ion beam microscopy and nanoindentation are utilised to probe the corrosion evolution of nanocomposite TiSiN coatings on steel substrates in nitric acid solution and unlock the controlling mechanism under which the coated steels corrode. The effect of residual stress upon localised corrosion development is also clarified by finite element analysis. Accordingly, new strategies are proposed to extend the service life of ceramic coatings in corrosive environments.

It will be really appreciated, if you kindly publish this manuscript in your renowned journal.

Regards.

On behalf of all Authors,

Mohammad S Ahmed

Edith Cowan University

***Research Highlights**

- Pitting, originated from surface defects, was dominant in TiSiN coated steels,
- Thin oxidation layer generated by annealing provided protection against corrosion,
- Compressive residual stress resisted corrosion propagation in TiSiN coated steels.

Corrosion behaviour of nanocomposite TiSiN coatings on steel substrates

Mohammad Shoeb Ahmed[a], Paul Munroe[b], Zhong-Tao Jiang[c], Xiaoli Zhao[a], William Rickard[d], Zhi-feng Zhou[e], Lawrence Kwok Yan Li[e] and Zonghan Xie[a,*]

[a]School of Engineering, Edith Cowan University, Joondalup, WA 6027, Australia

[b]School of Materials Science and Engineering, University of New South Wales, NSW 2052, Australia

[c]School of Engineering and Energy, Murdoch University, Western Australia 6150

[d]Department of Imaging and Applied Physics, Curtin University of Technology, WA6102, Australia

[e]Advanced Coatings Applied Research Laboratory (ACARL), Department of Manufacturing Engineering and Engineering Management, City University of Hong Kong, China

* Corresponding author: Zonghan Xie, School of Engineering, Edith Cowan University, Joondalup, WA 6027, Australia; Phone: 61 8 6304 5062, Fax: 61 8 6304 5811, email: z.xie@ecu.edu.au

Abstract

Nanocomposite TiSiN coatings were deposited on tool steels. Detailed mechanisms that govern the corrosion of these coated steels were revealed, following immersion tests in 70% nitric acid solution. Pitting occurred preferentially at surface defect sites and expanded with increasing immersion time. Both Young's modulus and hardness decreased as the corrosion damage intensified. A thin oxide layer formed during thermal annealing at 900°C was found to be effective against corrosive attack. In addition, compressive residual stress was noted to suppress the propagation of corrosion-induced cracks. Role of residual stress in controlling the corrosion resistance of these ceramic-coated steels was clarified.

Keyword: Nanocomposite coatings, corrosion, residual stress, focused ion beam microscopy, finite element analysis

1. Introduction

Nanocomposite ceramic coatings have been investigated intensively in recent years for applications in machining tools and medical devices, owing to their high hardness and good wear resistance [1-4]. Among them, TiSiN is commonly applied. Pitting corrosion has been frequently observed in ceramic coatings deposited on steel substrates, originating from surface defect sites [5,6,]. Electron microscopy, surface X-ray diffraction (XRD) and X-ray photoelectron spectroscopy have been used to probe the mechanisms under which these ceramic coated steels corroded [7, 8, 9]. However, a detailed understanding of initiation and propagation of corrosion in surface-treated steels is lacking and, consequently, the factors that control the expansion of pitting remains unclear. Though mechanical properties of ceramic coatings are anticipated to deteriorate during corrosion, no data are available to date to substantiate such a hypothesis, making it difficult to predict the service life of ceramic coated steels in corrosive environments.

High compressive residual stress is known to exist in ceramic coatings prepared by PVD [10, 11]. Although, stress corrosion cracking has often been observed in metals subjected to tensile stresses [12], little effort has been made so far to clarify the effect of compressive residual stress on the corrosion behaviour of ceramic-coated steels. Focused ion beam (FIB) microscopy is a powerful tool in the preparation and analysis of local cross-sections in a

material surface [13, 14]. It has recently been used for subsurface characterization of ceramic coatings following mechanical surface testing [15, 16]. In this study, FIB, along with XRD, X-ray photoelectron spectroscopy (XPS) and nanoindentation testing, were used to characterise the microstructural evolution in both surface and subsurface after corrosion tests and determine key factors that control the corrosion process. The change of mechanical properties of the coatings under the influence of corrosion was quantified, and the effect of residual stress on the corrosion progression was also clarified by finite element analysis (FEA).

2. Experimental procedure

2.1 Sample preparation

Nanocomposite TiSiN coatings were deposited onto AISI M42 tool steel substrates by physical vapour deposition (PVD) using a reactive close-field unbalanced magnetron sputtering system (UDP650, Teer Coatings Ltd., Droitwich, Worcestershire, UK). The details of the deposition procedure were given elsewhere [17] and can be summarised as follows: prior to deposition, the surface of the steel substrates was bombarded by Ar ions to remove the oxide layer and other contaminants. During deposition a Ti buffer layer of ~0.2 μm was first deposited, followed by a TiN transition layer of ~1 μm. The thickness of the outer TiSiN coating was ~3 μm and it was composed of ~50 at.% of Ti, ~10 at.% of Si and ~40 at.% of N, as determined by XPS. After deposition, some of the samples were annealed for 3 hours in a Carbolite vacuum tube furnace at 900 °C with a base pressure < 1×10^{-6} Torr and a heating rate of 5°C/min. Compressive residual stress in as-deposited TiSiN coatings was found to decrease from ~10 GPa to ~1 GPa after the thermal annealing treatment [18]. However, the

microstructural features of the annealed samples remained identical to that of the as-deposited specimens, as shown in Figure 1.

2.2 Corrosion tests

Before immersion tests, the samples were coated with an acrylic protective layer (without metallic flakes) to expose only the coated area. The tests were performed in 70% HNO_3 solution at 25°C. The immersion period was set as 2 and 8 days.

2.3 Surface structure characterisation

The coating crystal structure of all the samples was characterised by grazing incidence XRD (GI-XRD) at the powder diffraction beam line of the Australian Synchrotron located in Melbourne, Australia. The energy of the synchrotron radiation was 9.0 keV, which corresponds to a wavelength of 0.13 nm at an incidence angle of 1°. The patterns were collected over the 2θ range of 20° to 80°. The depth of the incidence SR beam was 0.5 μm, according to a formula described elsewhere [19].

The surface bonding structure of both virgin and corroded TiSiN coatings were probed by XPS (Kratos Axis Ultra XPS spectrometer, Manchester, UK) with Mg Kα radiation (hν = 1,253.6 eV). The sample was mounted horizontally normal to the entrance of electrostatic lens. The base pressure of the analyser chamber was maintained at ~10^{-9} Torr. The voltage and emission current of X-ray source were kept at 12 kV and 12 mA, respectively. The pass energy were selected at 80 eV for survey scan and 10 eV for the features of interests (i.e., N1s, Ti2p, Si2p) to ensure high resolution and good sensitivity. XPS spectra energy scale was

calibrated using Cu2p (932.67 eV), Ag3d (368.27 eV), C1s (284.6 eV) and Au4f (83.98 eV). The electrostatic lens mode and analyser entrance were selected Hybrid and Slot mode (Iris = 0.6 and Aperture = 49), respectively. A charge neutraliser was employed during the XPS measurements.

2.4 Surface and subsurface observations

Sectioning and imaging of the surface defects of virgin annealed samples were conducted on a Neon 40EsB focussed ion beam scanning electron microscope (FIB-SEM) (Carl Zeiss NTS GmbH, Oberkochen, Germany). Imaging of the subsurface was achieved using the FIB to expose a cross-section of the sample. Images were collected using an in-lens secondary electron detector. The surface of both virgin and corroded samples was examined using a field emission scanning electron microscope (FESEM) (Model Fei Nova 230, EI Company, Hillsboro, OR, USA). Sectioning and subsurface imaging of samples was also carried out using a focused ion beam (FIB) workstation (FEI xP200 focused ion beam microscope, FEI Company, Hillsboro, OR, USA). The procedure has been described elsewhere [20]. First, a high gallium ion beam current (7,000 pA) was used to mill through the surface area of interest and to create a wedge-like trench. The resultant rough cross-section was then polished at medium currents (1,000 – 3,000 pA) to remove particle deposition and smooth the surface. Finally, the cross section was imaged at lower beam currents.

2.5 Nanoindentation testing

A nanoindentation system (Ultra-Micro Indentation System 2000, CSIRO, Sydney, Australia), equipped with a Berkovich indenter, was used to measure the mechanical

properties of the TiSiN coatings before and after corrosion tests, according to a standard method [21]. Prior to nanoindentation testing, the area function of the indenter tip was calibrated using a fused silica specimen. Nanoindentation tests were carried out under load control with a maximum load of 50 mN. For each test, 20 incremental and 20 decremental steps were used. The maximum penetration depth during the tests was found to be less than 10 % of the TiSiN coating thickness, which ensured only the coating properties were measured.

2.6 Finite element analysis of residual stress distribution

An axisymmetric model (Comsol Multiphysics software, Version 3.5a, Burlington, MA 01803, USA) was constructed to create a direct link between the residual stress and corrosion resistance. The model that contains the cross section of a cone-shaped cavity, resulting from localised corrosion damage, is shown in Fig.2. The geometry and size of the corrosion damage site in the model are based upon the subsurface observations enabled by the FIB microscopy. Boundary conditions are given as follows: the left hand side is the axisymmetric axis. The bottom and the right hand side are fixed along the z and r directions, respectively, but free to move in the other directions. The overall dimension of the model is much larger than both the thickness of the coating layers, and the edge effect due to boundary constrains is thus negligible. The meshes were generated in an interactive way to ensure that they were sufficiently dense around the edge, which defines the inner wall of the corrosion cavity. Planar compressive residual stresses were assigned to the TiN and TiSiN layers. For the as-deposited samples, the residual stresses were set to be 3 GPa for the TiN layer [22] and 10 GPa for the TiSiN layer [18]. For the annealed samples, the residual stresses were set to be 0.3 GPa and 1 GPa for the TiN and TiSiN layers, respectively [18]. Under the influence of

the residual stress, the percent reduction in the cavity area sectioned along the horizontal direction at a distance of x from the cavity tip can be calculated by $\delta A/A = (r_0^2(x) - r^2(x)) / r_0^2(x)$, where r(x) and $r_0(x)$ are the radii of the cavity area under stress and stress-free conditions, respectively. Structural and physical parameters of both the substrate and coating materials are given in Table I.

3. Results

3.1 Characterisation of surface crystal structure

The surface crystal structure of the as-deposited and annealed samples were analysed by GI-XRD before and after corrosion tests. Four diffraction peaks identified at the diffraction angles of 32.5°, 39.9°, 64° and 72° corresponded to {1 1 1}, {2 0 0}, {2 2 0} and {3 1 1} crystal planes of cubic B1 NaCl-type TiN, respectively (Fig. 3(a) & (b)). Notably, with the increase of immersion test time, the TiN {1 1 1} peak was intensified, indicative of a continuing removal of the outer nanostructured TiSiN layer and the exposure of the columnar-grained TiN transitional layer having a preferred {1 1 1} orientation [23]. In addition, the peaks of austenite phase (γ) {200} and martensite phase (M) {200} of M42 steel substrate appeared in both types of virgin samples, suggesting that surface defects such as pits may exist in the samples. The peaks of these steel phases were intensified with increasing immersion time, most likely due to the thinning or removal of the coating under acid attack. The other small peaks were associated with the carbide phases of M42 steel substrate. No diffraction peaks related to Si and its compounds were identified. By comparing the peak intensity of both γ and M phases, the as-deposited coating seemed to be more

susceptible to corrosion attack than the annealed samples, though both coatings exhibited a similar trend in the evolution of peak intensity.

3.2 Analysis of the surface chemistry of the coatings

The change in surface chemical bonding states of both as-deposited and annealed samples with the development of corrosion progress were characterised by XPS. From N 1s spectra, the two peaks at ~396 eV and ~397 eV arise from Ti-O-N and TiN phases, respectively, whereas the other peak at 400 eV represents Si_3N_4 (Fig. 4(a) & (b)). Considering that no crystalline Si_3N_4 phase was detected in the samples during GI-XRD analysis (Fig. 3), Si_3N_4 was thought to exist in an amorphous state in TiSiN coatings [24]. The peak of Ti–O–N might be attributed to surface contamination caused by oxygen [25, 26]. By increasing the immersion period to eight days, the intensities of these peaks decreased significantly, presumably due to aggressive attack of the nitric acid on the samples. According to the Ti 2p spectra, two pairs of peaks from Ti 2p3/2 and Ti 2p1/2 were identified before and after the immersion tests, corresponding to TiN and TiO_x phases in the surface of both as-deposited and annealed samples (Fig. 4(c) & (d)). Prior to the corrosion tests, TiO_x prevailed in the annealed sample, while TiN phase was dominant in the as-deposited sample, indicating that an oxidation layer formed during the thermal treatment at 900°C. Following two days immersion tests, TiO_x remained dominant in the annealed sample. However, surface passivation seemed to occur in the as-deposited sample, making TiO_x the dominant phase. With increasing immersion time up to eight days, the intensities of these peaks decreased for both phases, indicating corrosion progression in the acid solution. Analysis of the binding energy peaks associated to Si 2p spectra shows only one peak at 102.7 eV corresponding to

Si_3N_4 phase in both as-deposited and annealed samples (Fig. 4(e) & (f)), whose intensities also decreased with the increase of immersion time in the acid solution. The binding energies of surface phases identified by XPS in the samples before and after corrosion tests are given in Table II.

3.3 Nanoindentation tests

Young's modulus and hardness of the as-deposited sample were found to be higher than the annealed sample by ~25% and ~47%, respectively, before immersion tests (Fig. 5). A slight decrease of mechanical properties was observed for both types after two days immersion tests. By immersing the samples in 70% HNO_3 solution for eight days, the as-deposited sample showed a marked decrease in mechanical properties compared to the annealed: for Young's modulus, the as-deposited sample decreased by ~33% and the annealed sample by ~10% (Fig. 5(a)); for hardness, the as-deposited sample decreased by ~ 62% and the annealed samples by ~21% (Fig. 5(b)).

3.4 Surface and subsurface observations

The surface of both as-deposited and annealed coatings was examined before corrosion tests. Surface defects, such as micron-sized pits and embedded particles, were observed in both samples (Fig. 6(a)&(b)). Elemental maps, recorded using EDS, over a surface pit in Fig. 6(b) were also acquired. The colour pixels in these images represent the presence of the elements

of interest. Notably, a high concentration of iron was detected within the pit, indicating that the steel substrate may be locally exposed and more likely to corrode in subsequent immersion tests. To probe the depth of a surface pit, a cross-section was produced across the pit (Fig. 6(c)). The pit was observed to have a depth to the thickness of the TiSiN coating. Within the pit, micron-sized particles can also be seen, apparently arising from the deposition process.

The sample surface was examined following two and eight-days immersion tests (Fig. 7). For samples subjected to two days corrosion tests, the initiation of localised corrosion was observed at surface defect sites. By increasing the immersion time to eight days, pitting was observed to expand in both types of coated specimens – moving downward and corroding the less-noble steel substrate, and at the same time propagating laterally along the interface between the outer TiSiN coating and the TiN underlayer. More often, pits extended to join their neighbours in the as-deposited sample and created widespread damage in the coatings, compared to a relatively isolated pitting damage in the annealed sample. Elemental maps over two pits in the annealed sample were also given after 8 days immersion tests; the steel substrate was more evident inside the pits than in the virgin samples.

To clarify the effect of compressive residual stress in the coatings on the corrosion behaviour of the coated seels, the cross-sections of the coating samples were prepared after corrosion tests and the interaction between the coating microstructure and corrosion progression was examined (Fig. 8). For two days immersion tests, the lateral expansion of the pits along the TiSiN/TiN interface was observed in both types of TiSiN coatings, since the TiN layer within the pits acted as a physical barrier against downward progression of corrosion. Even so,

corrosion penetration through the less-densely packed boundaries between vertically aligned columnar TiN grains was evident in the annealed coating. Following eight days immersion tests, an appreciable thinning of the TiN layer was observed at the pitting sites in the as-deposited sample, caused by prolonged acid attack. Neither subsurface cracks nor delamination were noted. In contrast, the exposed TiN layer was etched away in bulk at the pitting sites in the annealed sample (Fig. 9). Moreover, delamination was detected at the interface between the top TiSiN and TiN as well as the boundary between the TiN and steel substrate around these pitting sites.

3.5 Effect of residual stress on the corrosion resistance

A FEA model was constructed to quantify the effect of compressive residual stress on the opening of corrosion-induced cavities in the samples. The percent reduction of lateral section area of a cavity was observed to increase rapidly with the opening (i.e. the size of end diameters) of the cavity (Fig. 10). For a through-TiN coating cavity the maximum area reduction was ~3% (Fig. 10(a)), while the reduction was larger for a shallow cavity, i.e., ~ 8% (Fig. 10(b)), meaning that the residual stress was more effective in resisting the infiltration of corrosive agents at the early stage of corrosion development. Moreover, the maximum percent area reduction was noted to occur near the cavity tip, in particular for the shallow cavities, indicating the residual stress played a critical role in resisting the corrosion advance.

4. Discussion

The effect of the coating microstructure and residual stress on the corrosion behaviour of TiSiN coated steels in acidic environments was investigated in this work. The microstructure of these coatings consisted of three sublayers, namely, a nanocomposite TiSiN outer layer, a columnar-grained TiN transitional layer and a thin metallic Ti adhesion layer. All these three layers, while fulfilling their mechanical functions, also acted as physical barriers against potential corrosion attack on the steel substrates. Surface imperfections, such as pinholes and microparticles, are often found in PVD prepared ceramic coatings [27, 28], and these defects played an important role in the initiation and expansion of corrosion damage in the coatings in corrosive solutions [29, 30]. Unlike previous studies on corrosion of ceramic-coated steels, in which a understanding of corrosion mechanism was mainly developed from the surface observation [31, 32, 33], direct subsurface observation was conducted in this work, in combination with a host of surface characterisation techniques including FESEM, GI-XRD, XPS and nanoindentation. Detailed mechanistic insights into the mechanism that controlled the corrosion behaviour of ceramic coatings on steel substrates were thus gained.

Compressive residual stress, as high as ~10 GPa, was measured for the as-deposited TiSiN coatings [18], and its origins and effects upon the mechanical behaviour of the coatings have recently been explored [17, 18]. The magnitude of residual stress in the as-deposited coatings can be reduced to ~1 GPa by thermal annealing at 900°C [18]. Interestingly, this treatment has little impact upon the composition and microstructure of the TiSiN coatings, except that a thin oxide layer formed on the surface of TiSiN coatings. The newly formed layer was noted to act as a barrier to restrict lateral expansion and merging of localised corrosion. It may

explain why the annealed samples showed greater Young's modulus and hardness than the as-deposited after eight days corrosion tests.

Compressive residual stress in the coatings also played a key part in resisting the corrosion damage in the coated steels. The propagation of cracks induced by localised corrosion was suppressed by high compressive residual stress in the as-deposited coatings. In contrast, by diminishing compressive residual stress through thermal annealing, the corrosion cracking occurred with little resistance preferentially through structural defects, i.e., the boundaries of exposed columnar TiN grains and the interface between sublayers, causing appreciable damage around the pits. Moreover, the FEA model demonstrated that compressive residual stress can reduce the size of cavities created by corrosive attack, leading to an increase in corrosion resistance.

5. Conclusions

Direct subsurface observation, in combination with surface characterisation and modelling techniques, was performed to probe the corrosion evolution of TiSiN coated steels in 70% nitric acid, with a focus on the roles of surface oxidation layer and compressive residual stress in controlling the development of localised corrosion. The following conclusions can be drawn:

1) Corrosion pitting was observed to be dominant in TiSiN coatings on steel substrates, which originated from surface defects.

2) Thin oxidation layer, formed during post-deposition annealing treatment, inhibited the penetration of acidic solution through the surface of the annealed coating and provided an overall protection of the coated steels.
3) Compressive residual stress suppressed the propagation of corrosion-induced cracks through the sublayer interface and the boundaries of columnar TiN grains and helped maintain the structural integrity of TiSiN coated steel systems.

Accordingly, surface oxidation technique may be applied in conjunction with the control of compressive residual stress to provide an effective protection against localised corrosion in PVD-prepared ceramic coatings on steels.

Acknowledgement

This work is supported by the 2010 ECU-Industry Collaboration Scheme and the Innovation and Technology Fund (ITF) of Hong Kong (Project No. 9440052 (ITS/082/06)). MS Ahmed acknowledges an Australian Postgraduate Award that supports his PhD study and a 2010 travel grant (TAP 9029) offered by the Australian Microscopy & Microanalysis Facility (AMMRF) for FIB work. ZH Xie acknowledges a 2010 travel grant offered by the Australian Synchrotron (AS) for access to power diffraction beamline.

References

1. D. M.-Martínez, C. L.-Cartes, A. Fernández, J.C. Sánchez-López, Influence of the microstructure on the mechanical and tribological behavior of TiC/a-C nanocomposite coatings, Thin Solid Films. 517 (2009) 1662–1671.

2. Y.H. Cheng, T. Browne, B. Heckerman, E.I. Meletis, Mechanical and tribological properties of nanocomposite TiSiN coatings, Surf. Coat. Technol. 204 (2010) 2123–2129.

3. Z. Zeng, Y. Zhou, B. Zhang, Y.L. Sun, J. Zhang, Designed fabrication of hard Cr-Cr2O3-Cr7C3 nanocomposite coatings for anti-wear application, Acta Mater. 57 (2009) 5342–5347.

4. J. Lin, J. J. Moore, B. Mishra, M. Pinkas, W. D. Sproul, The structure and mechanical and tribological properties of TiBCN nanocomposite coatings, Acta Mater. 58 (2010) 1554–1564.

5. X. Z. Ding, A. L. K.Tan, X. T. Zeng, C.Wang, T. Yue, C. Q.Sun, Corrosion resistance of CrAlN and TiAlN coatings deposited by lateral rotating cathode arc, Thin Solid Films. 516 (2008) 5716–5720.

6. C. L. Chang, C. T. Lin, P. C. Tsai, W. Y. Ho, W. J. Liu, D. Y Wang, Mechanical and corrosion properties of (Ti,Si)N coating synthesized by cathodic arc plasma evaporation, Surf. Coat. Technol. 202 (2008) 5516-5520.

7. Y.-Y.Li, F.-B.Wu, Microstructure and corrosion characteristics of CrN/NiP sputtering thin films, Thin Solid Films. 518 (2010) 7527-7531.

8. Y. Wang, W. Tian, T. Zhang, Y.Yang, Microstructure, spallation and corrosion of plasma sprayed Al2O3-13%TiO2 coatings, Corros. Sci. 51 (2009) 2924-2931.

9. L. Wang, D.O. Northwood, X. Nie, J. Housden, E. Spain, A. Leyland, A. Matthews, Corrosion properties and contact resistance of TiN, TiAlN and CrN coatings in simulated proton exchange membrane fuel cell environments, J. Power Sources. 195 (2010) 3814-3821.

10. S.J. Suresha, R. Gunda, V. Jayaram, S.K. Biswas, Effect of residual stress on the fracture strength of columnar TiN films, J. Mater. Res. 22 (2007) 3501-3506.

11. Z.J. Liu, N. Jiang, Y.G. Shen, X. Li, Stress-induced surface damages in Ti–Si–N films grown by magnetron sputtering, Thin Solid Films. 516 (2008) 7609-7614.

12. T. Allen, J. Busby, M. Meyer, D. Pett, Materials challenges for nuclear systems, Mater. Today. 13 (2010) 14-23.

13. Z. -H. Xie, M. Hoffman, R. J. Moon, P. R. Munroe, Y.-B. Cheng, Subsurface Indentation Damage and Mechanical Characterization of α-SiAlON Ceramics, J. Am. Ceram. Soc. 87 (2004) 2114-2124.

14. Z. -H. Xie, R. Moon, M. Hoffman, P. Munroe, Y.-B. Cheng, Microstructural Effect on Grinding and Polishing of α-SiAlON Ceramics, J. Euro. Ceram. Soc. 23 (2003) 2351-2360.

15. Z. H. Xie, M. Hoffman, R. J. Moon, P. R. Munroe, Deformation of a hard coating on ductile substrate system during nanoindentation: Role of the coating microstructure, J. Mater. Res. 21 (2006) 437-447.

16. P.C. Wo, P.R. Munroe, Z.F. Zhou, K.Y. Li, Z.H. Xie, Effects of TiN sublayers on the response of TiSiN nanocomposite coatings to nanoidentation and scratching contacts, Mater. Sci. Eng., A 527 (2010) 4447-4457.

17. M. S. Ahmed, Z.-F. Zhou, P. R. Munroe, L.K.Y. Li, Z. Xie, Control of the damage resistance of nanocomposite TiSiN coatings on steels: roles of residual stress, Thin Solid Films. In press (2010) 1-13.

18. M.S. Ahmed, X. Zhao, Z.F. Zhou, P.R. Munroe, N.C.-Tan, L.K.Y.Li, Z. Xie, Effect of thermal annealing upon residual stress and mechanical properties of nanostructured TiSiN coatings on steel substrates, J. Am. Ceram. Soc. In press (2010) 1-6.

19. W.K. Pang, I.M. Low, B.H. O'Connor, Z.M. Sun, K.E. Prince, Oxidation characteristics of Ti3AlC2 over the temperature range 500–900° C, Mater. Chem. Phys. 117 (2009) 384–389.

20. P. C. Wo, P. R. Munroe, M.Vasiliev, Z. H. Xie, K. Alameh, V. Kotov, A novel technique for microstructure characterization of garnet films, Opt. Mater. 32 (2009) 315-322.

21. W.C. Oliver, G.M. Pharr, Measurement of hardness and elastic modulus by instrumented indentation:Advances in understanding and refinements to methodology, J. Mater. Res. 19 (2004) 3-20.

22. Y. Paleau, Generation and evolution of residual stresses in physical vapour-deposited thin films, Vacuum 61 (2001) 175-181.

23. I. Iordanova, P.J. Kelly, R. Mirchev, V. Antonov, Crystallography of magnetron sputtered TiN coatings on steel substrates, Vacuum 81 (2007) 830-842.

24. S. Veprek, M.G.J. Veprek-Heijman, R.F. Zhang, Chemistry, physics and fracture mechanics in search for superhard materials, and the origin of superhardness in nc-TiN/a-Si_3N_4 and related nanocomposites, J. Phys. Chem. Solids 68 (2007) 1161-1168.

25. N. Jiang, Y.G. Shen , Y.-W. Mai, T. Chan, S. C. Tung, Nanocomposite Ti–Si–N films deposited by reactive unbalanced magnetron sputtering at room temperature, Mater. Sci. Eng., B 106 (2004) 163–171.

26. A. Flink, M. Beckers, J. Sjolen, T. Larsson, S. Braun, L. Karlsson, L. Hultman, The location and effects of Si in $(Ti_{1-x}Si_x)N_y$ thin films, J. Mater. Res. 24 (2009) 2483-2498.

27. H. C. Barshilia, B. Deepthi, A. S. A. Prabhu, K. S. Rajam, Superhard nanocomposite coatings of TiN/Si3N4 prepared by reactive direct current unbalanced magnetron sputtering, Surf. Coat. Technol. 201 (2006) 329-337.

28. C.-L. Chang, J.-H. Chen, P.-C. Tsai, W.-Y. Ho, D.-Y.Wang, Synthesis and characterization of nano-composite Ti–Si–N hard coating by filtered cathodic arc deposition, Surf. Coat. Technol. 203 (2008) 619–623.

29. P.M. Perillo, Corrosion Behavior of Coatings of Titanium Nitride and Titanium-Titanium Nitride on Steel Substrates, Corrosion. 62 (2006) 182-185.

30. R. J. M.-Palma, M. Manso, J. M. M.-Duart, A. Conde, J. J. Damborenea, Corrosion behavior of sputter-deposited TiN thin films, J. Vac. Sci. Technol., A. 21 (2003) 1635-1638.

31. C.-L. Chang, W.-C. Chen, P.-C. Tsai, W.-Y. Ho, D.-Y.Wang, Characteristics and performance of TiSiN/TiAlN multilayers coating synthesized by cathodic arc plasma evaporation, Surf. Coat. Technol. 202 (2007) 987–992.

32. L.Ying, L.Qu, F.Wang, The electrochemical corrosion behavior of TiN and (Ti,Al)N coatings in acid and salt solution, Corros. Sci. 45 (2003) 1367–1381.

33. Q. Yang, F. Cai, L.R. Zhao, X. Huang, Improving corrosion resistance of CrTiAlN coating by post-deposition treatments, Surf. Coat. Technol. 203 (2008) 606–609.

Table captions

Table I Materials properties of substrate and coating components used in FEA simulations.

Table II Binding energy peaks of N 1s, Ti 2p and Si 2p and corresponding phases identified by surface XPS analysis in both as-deposited and annealed samples before and after 2 days immersion tests

Figure captions

Figure 1 Secondary electron micrographs showing the microstructure of (a) as-deposited and (b) annealed TiSiN coatings on steel substrates.

Figure 2 Coating architecture and meshes in a localised corrosion model. Note that a cone-shaped cavity through the thickness of the TiN layer. The left-hand side is the axisymmetric axis.

Figure 3 Grazing incidence X-ray diffraction patterns of (a) as-deposited and (b) annealed coating samples before and after immersion tests. Patterns have been offset for ease of viewing. Note "γ" stands for austenite phase and "M" for martensite phase.

Figure 4 Surface X-ray photoelectron spectroscopy spectra for both as-deposited and annealed sample before and after immersion tests: the chemical bonding states of N 1s in (a) as-deposited and (b) annealed samples; the chemical bonding states of Ti 2p in (c) as-deposited and (d) annealed samples; the chemical bonding states of Si 2p in (e) as-deposited and (f) annealed samples.

Figure 5 Variation of (a) Young's modulus and (b) hardness of both as-deposited and annealed TiSiN coatings with immersion test time.

Figure 6 Scanning electron micrographs showing the surface of (a) as-deposited and (b) annealed TiSiN coatings on steel substrates, and a gallium ion-induced secondary electron micrograph showing (c) the cross section of a surface pit in the annealed coating sample. Next to the surface image in (b) are an enlarged view of a surface pit and corresponding Ti and Fe elemental maps.

Figure 7 Scanning electron micrographs showing the surface of both as-deposited and annealed TiSiN coatings on steel substrates after corrosion tests. Next to the surface image of the annealed sample subjected to 8 days immersion test are a separate view of two separate surface pits and corresponding Ti and Fe elemental maps.

Figure 8 Secondary electron micrographs showing the progression of the corrosion in as-deposited and annealed TiSiN coatings on steel substrates. Note corrosion-induced crack propagation can be seen in the annealed samples.

Figure 9 Scanning electron micrograph showing typical damage pattern of corrosion pitting in the annealed sample subjected to eight days immersion test. Note TiN layer in the central region is removed and the delamination of the top TiSiN layer occurs, presumably caused by corrosion cracking along the weak TiSiN/TiN interface.

Figure 10 Percent reduction of the lateral section area of cone-shaped cavities having different end diameters developed in the TiN layer of the as-deposited samples as a function of the distance to the cavity front. Insets showing the profiles of the cavities. (a) A pit of 1 μm depth and (b) a shallow pit of 200 nm depth.

Table I

	Substrate	TiSiN	TiN	Ti
Young's modulus (GPa)	200†	510[18]	590‡	104†
Poisson's ratio	0.30†	0.20	0.25	0.34†
Residual stress, as-deposited (GPa)	-	10	3	-
Residual stress, annealed (GPa)	-	1	0.3	-
Thickness (μm)	-	1.78	1.00	0.22

†http://www.efunda.com/materials/alloys/

‡http://www.ceramics.nist.gov/srd/scd/Z00220.htm

Table II

Sample type		Binding Energy (eV) of N 1s	Phases	Binding Energy (eV) of Ti 2p3/2	Phases	Binding Energy (eV) of Ti 2p1/2	Phases	Binding Energy (eV) of Si 2p	Phase
As-deposited	virgin	396.3 397.7 400.5	Ti-O-N TiN Si_3N_4	456 458.5	TiN TiOx	460.8 464.3	TiN TiOx	102.6	Si_3N_4
	2 days immersion	396.4 397.5 399.5	Ti-O-N TiN Si_3N_4	456 458	TiN TiOx	461.2 463.8	TiN TiOx	102.8	Si_3N_4
Annealed	virgin	396.4 397.4 400	Ti-O-N TiN Si_3N_4	455.8 458	TiN TiOx	461.5 463.8	TiN TiOx	102.3	Si_3N_4
	2 days immersion	396.6 397.8 399.7	Ti-O-N TiN Si_3N_4	455.6 457.6	TiN TiOx	461.3 463.5	TiN TiOx	102.2	Si_3N_4

Fig. 1

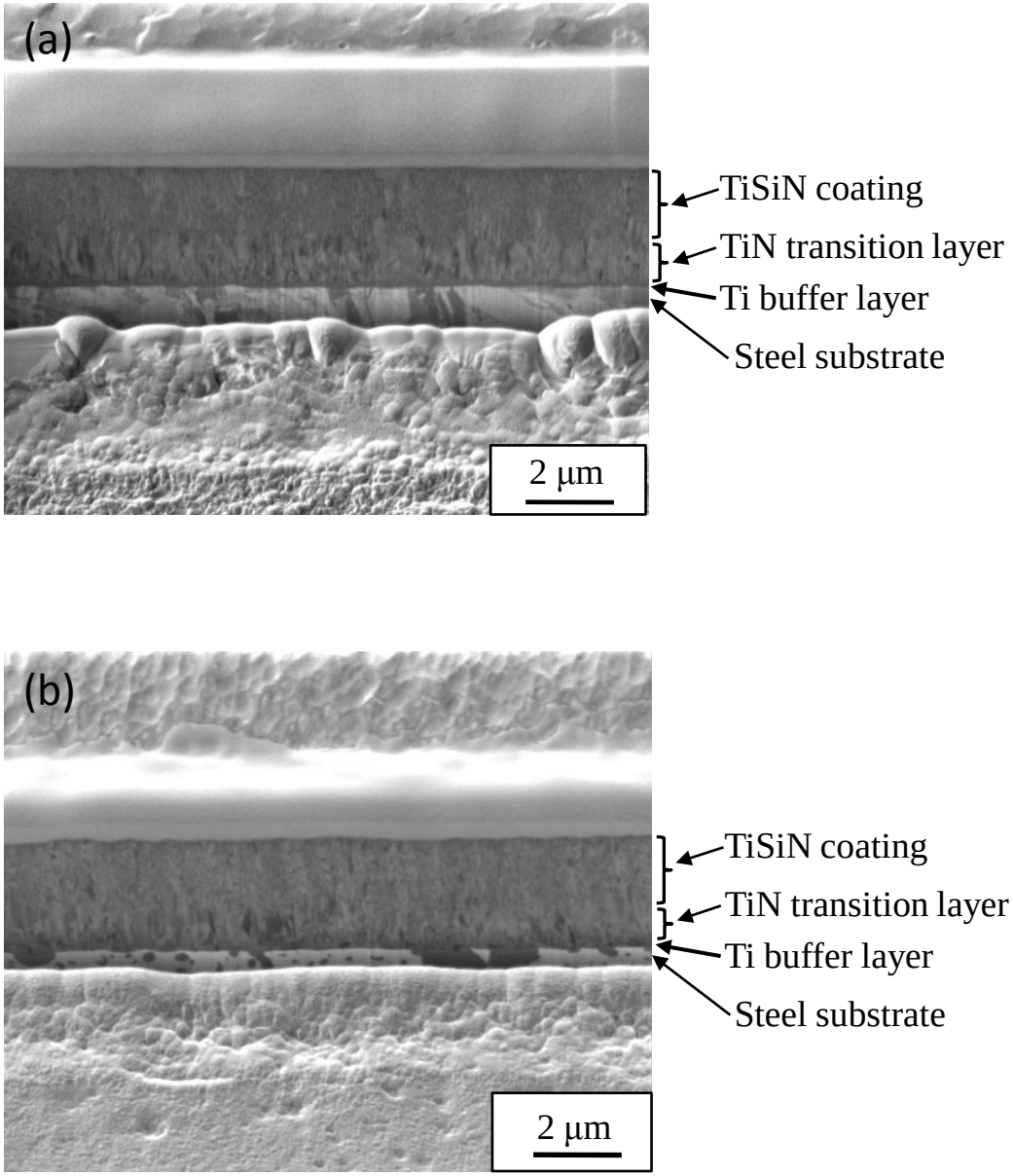
(a)
TiSiN coating
TiN transition layer
Ti buffer layer
Steel substrate
2 μm
(b)
TiSiN coating
TiN transition layer
Ti buffer layer
Steel substrate
2 μm

Fig. 2

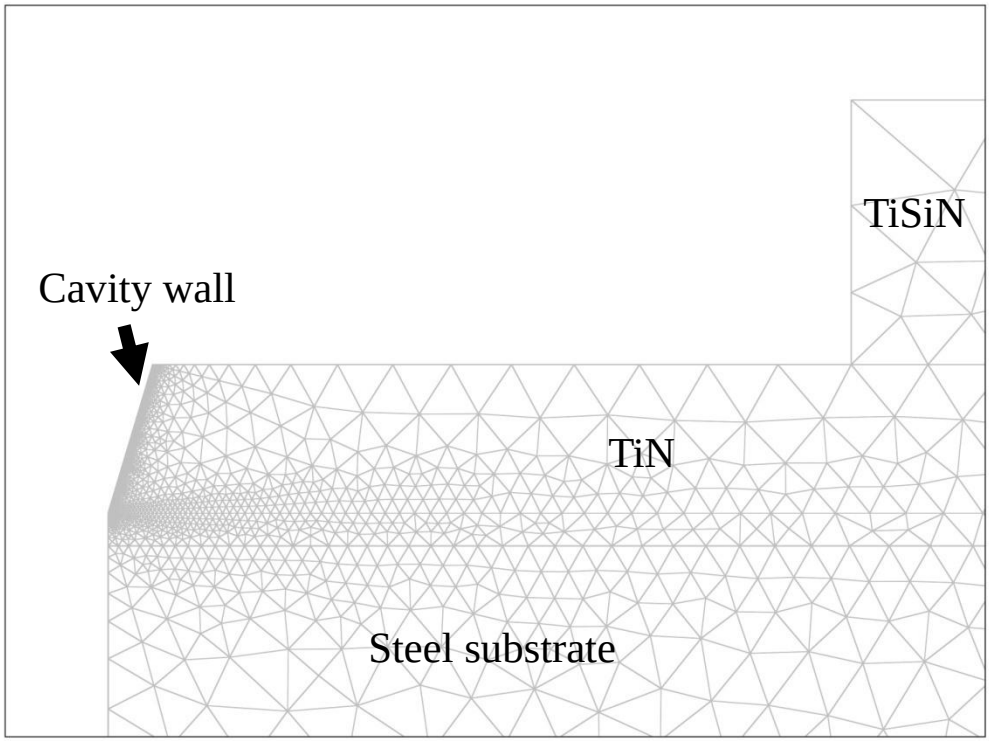

Fig. 3(a)

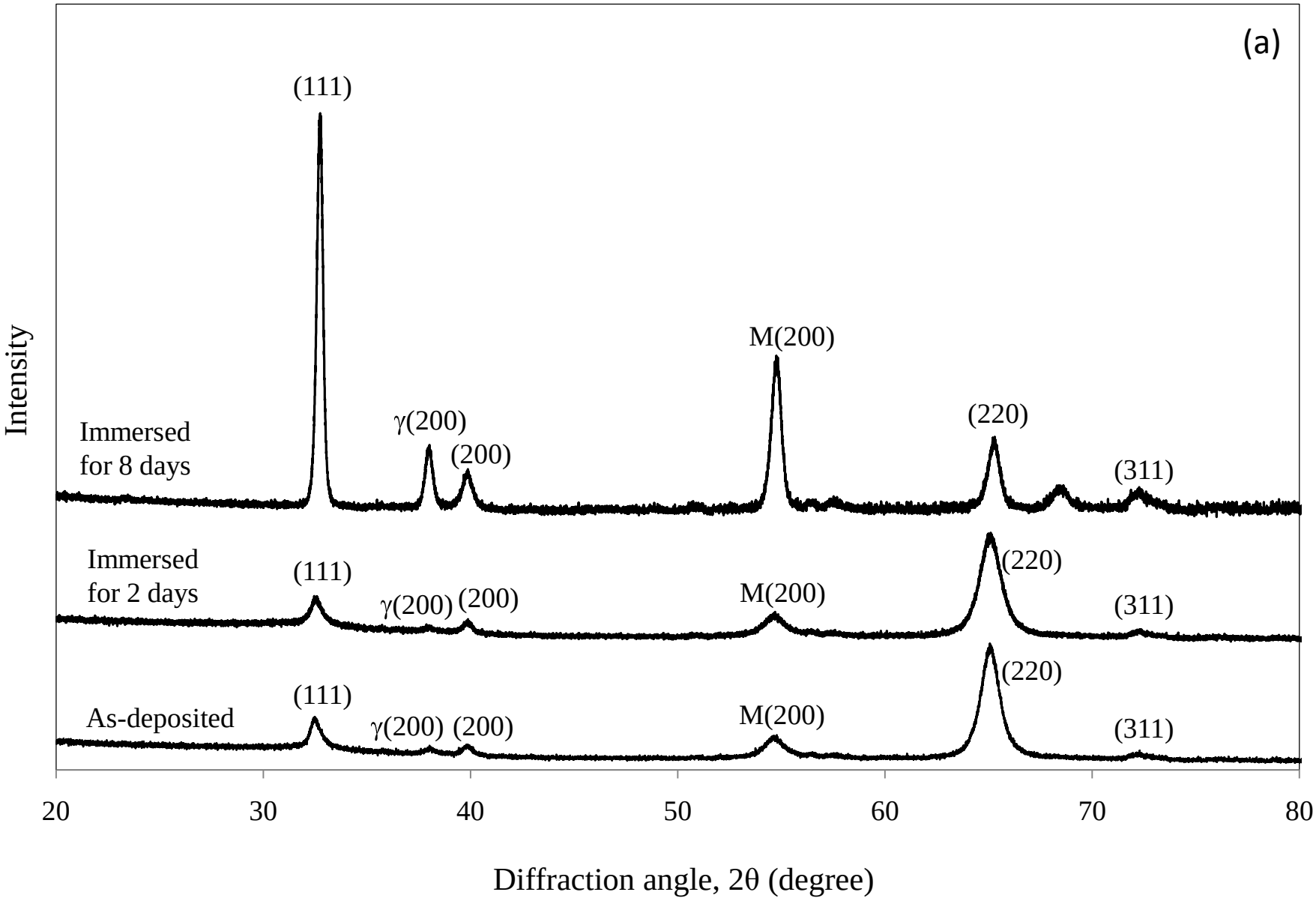
(a)
(111)
M(200)
(220)
γ(200)
(200)
(311)
Immersed for 8 days
Immersed for 2 days
As-deposited
Intensity
20
30
40
50
60
70
80
Diffraction angle, 2θ (degree)

Fig. 3(b)

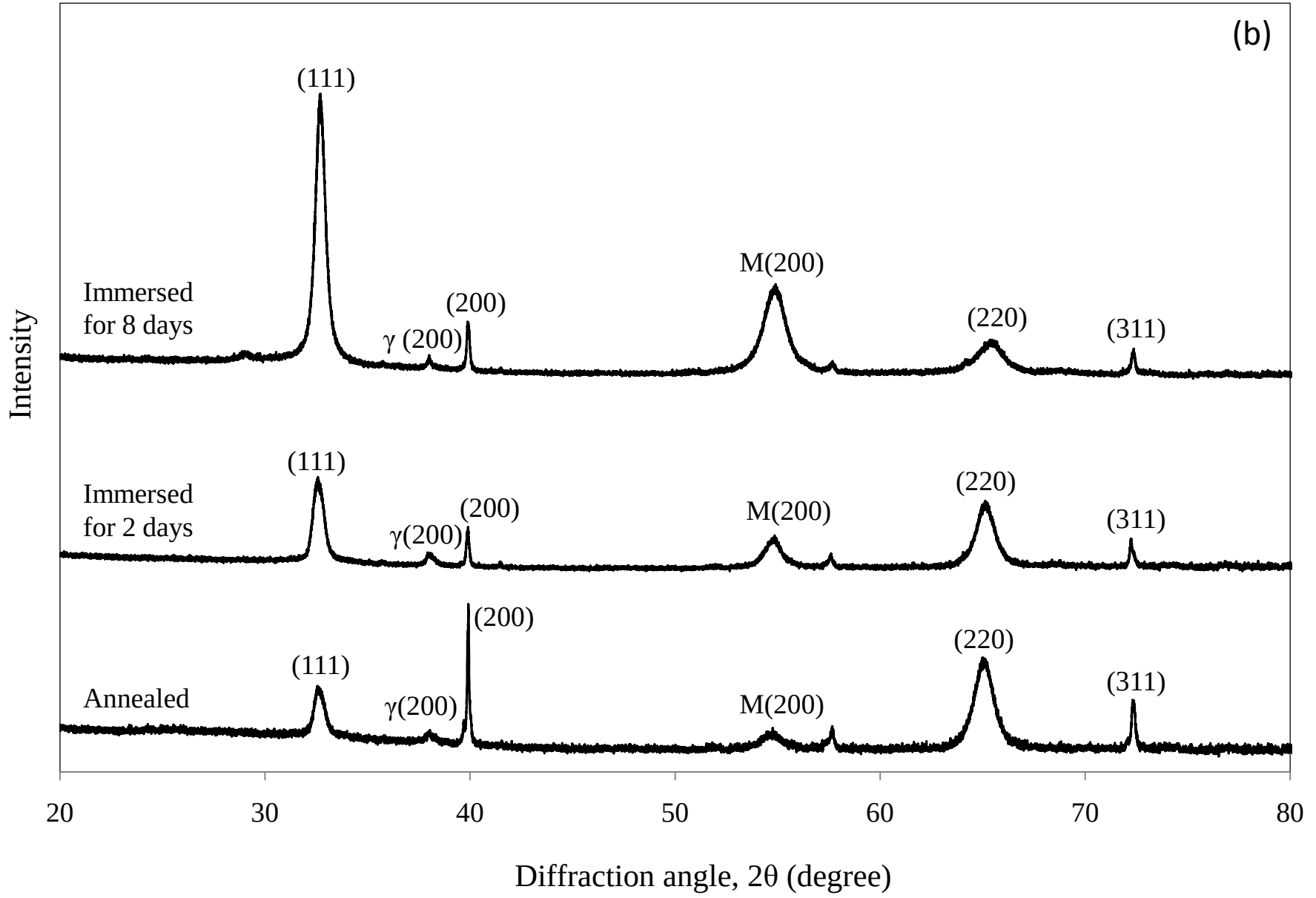
(b)
(111)
Immersed
for 8 days
γ (200)
(200)
M(200)
(220)
(311)
(111)
Immersed
for 2 days
γ(200)
(200)
M(200)
(220)
(311)
(200)
(111)
Annealed
γ(200)
M(200)
(220)
(311)
Intensity
20
30
40
50
60
70
80
Diffraction angle, 2θ (degree)

Fig. 4(a)

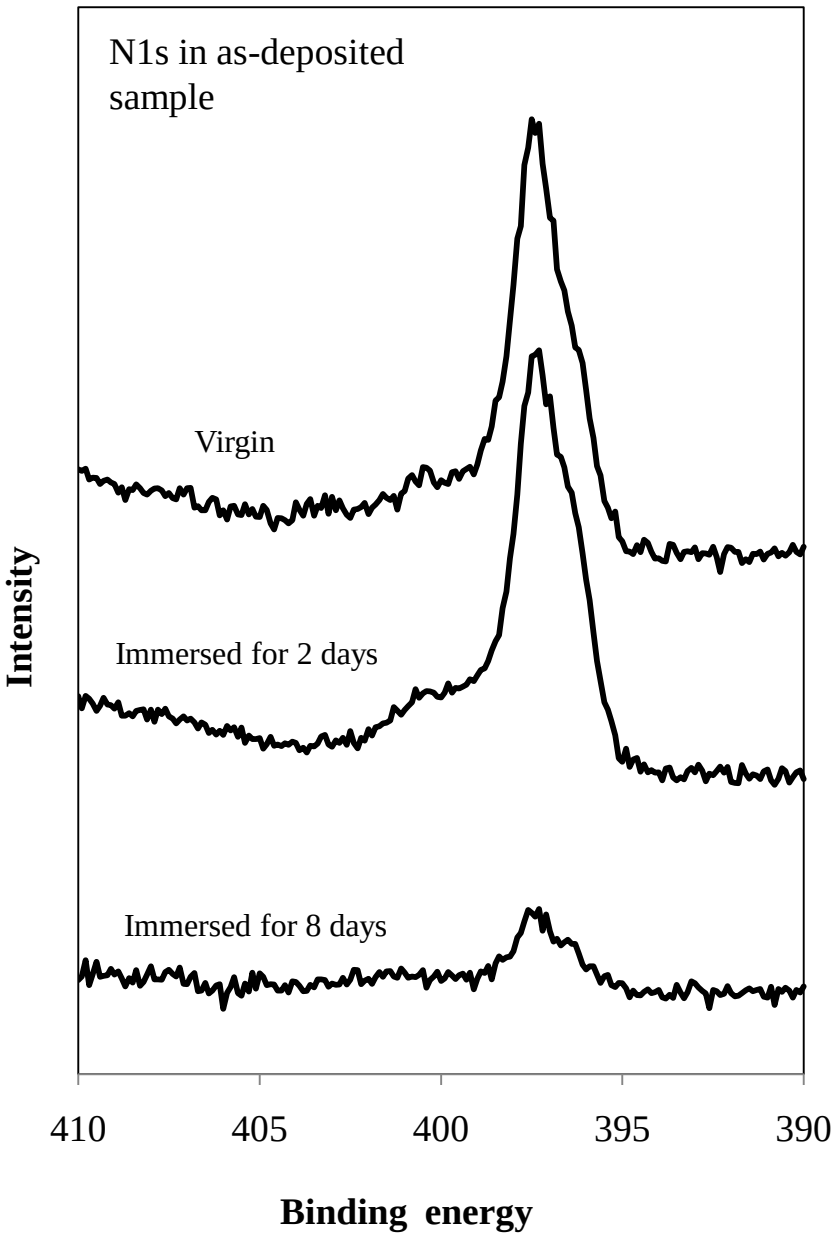
N1s in as-deposited sample
Virgin
Immersed for 2 days
Immersed for 8 days
Intensity
410
405
400
395
390
Binding energy

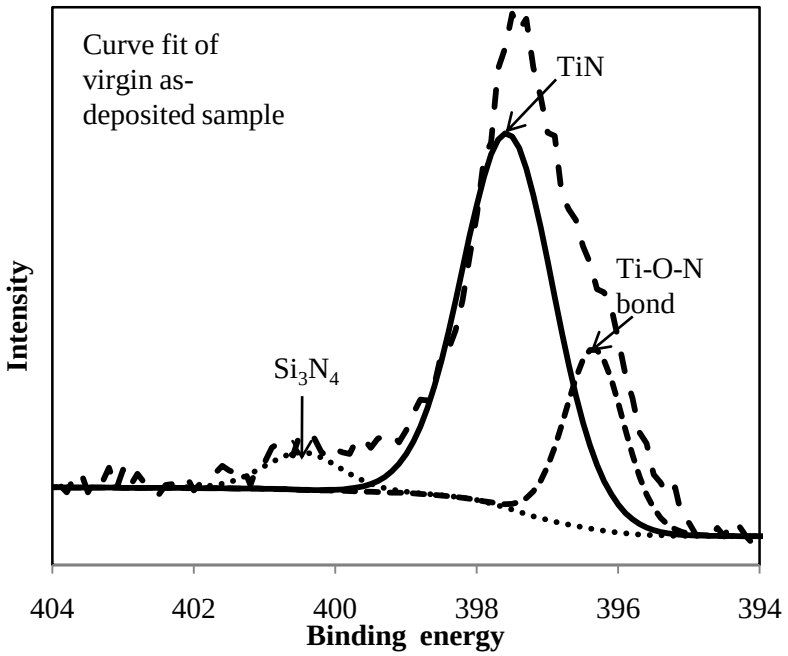
Curve fit of virgin as-deposited sample
TiN
Ti-O-N bond
Si_3N_4
Intensity
404
402
400
398
396
394
Binding energy

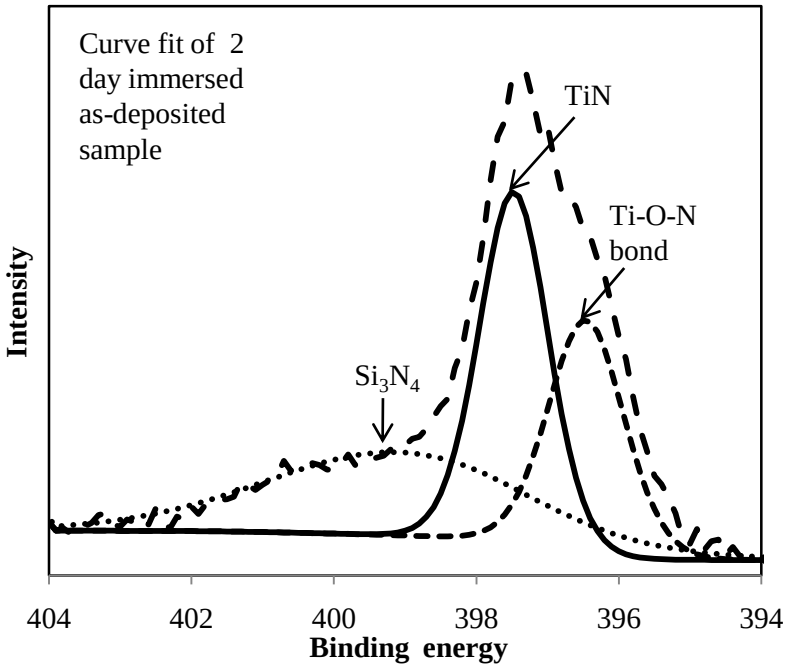
Curve fit of 2 day immersed as-deposited sample
TiN
Ti-O-N bond
Si_3N_4
Intensity
404
402
400
398
396
394
Binding energy

Fig. 4(b)

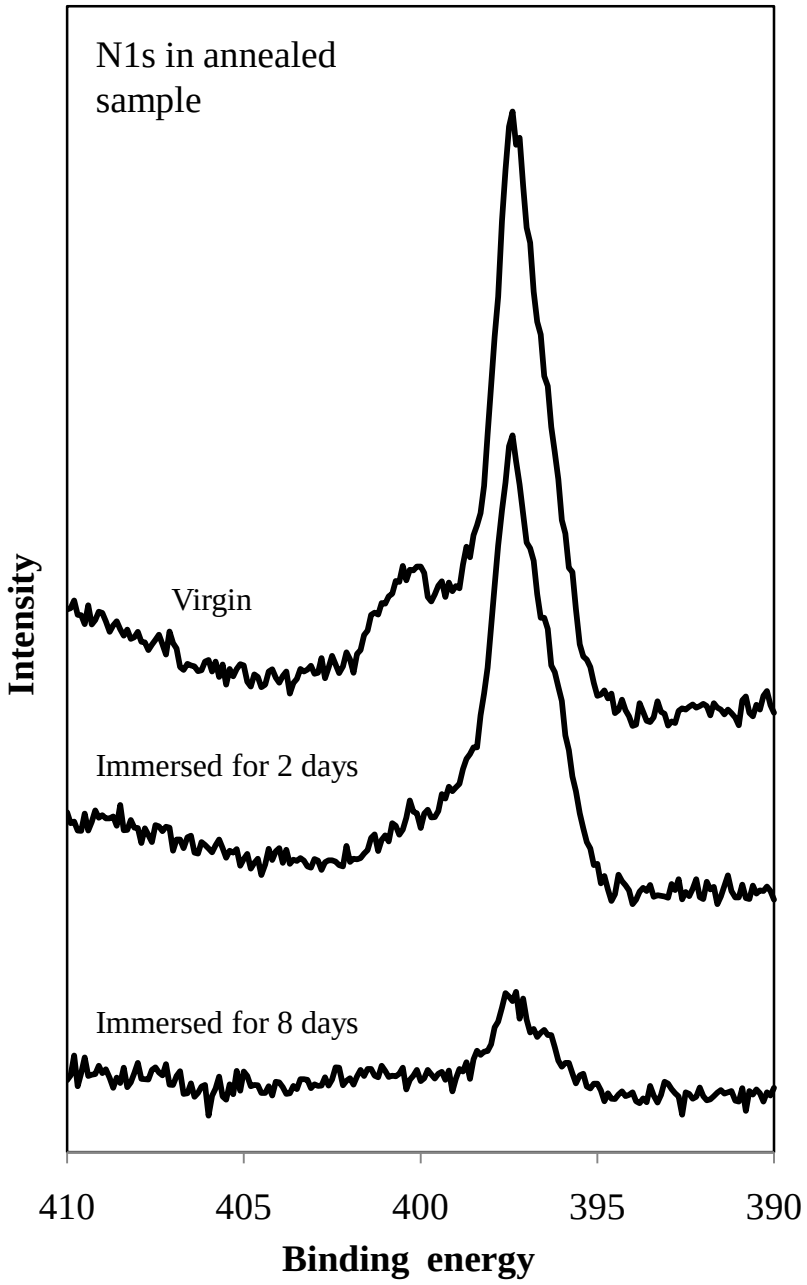
N1s in annealed sample
Intensity
Virgin
Immersed for 2 days
Immersed for 8 days
410
405
400
395
390
Binding energy

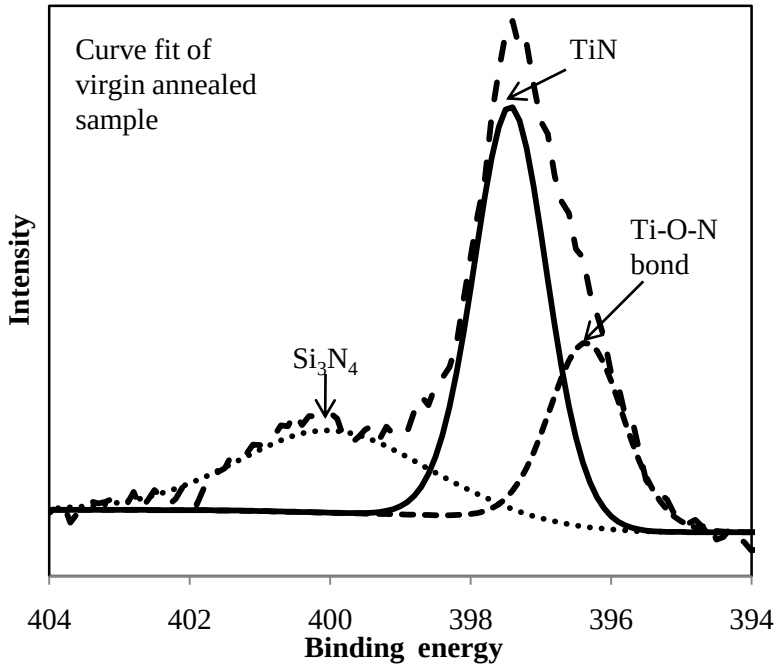
Curve fit of virgin annealed sample
TiN
Ti-O-N bond
Si3N4
Intensity
404
402
400
398
396
394
Binding energy

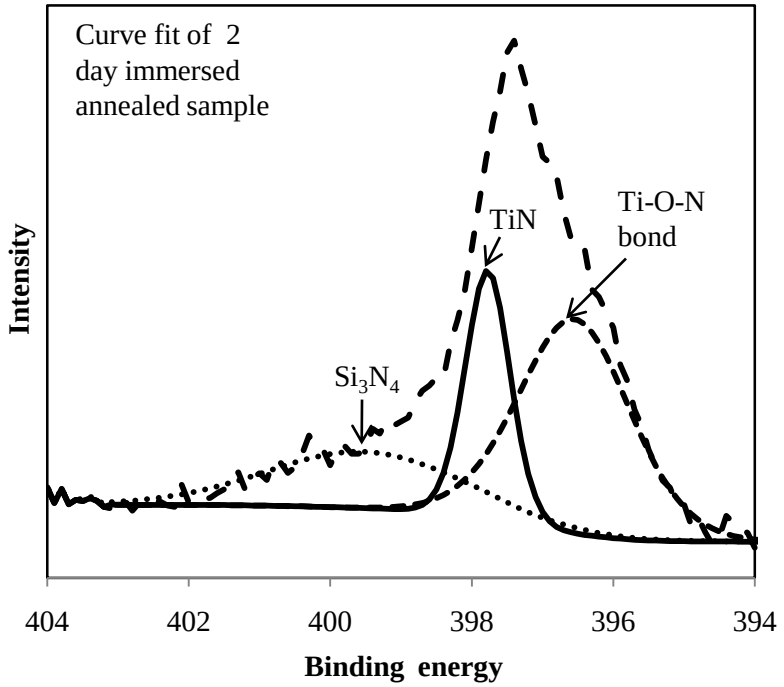
Curve fit of 2 day immersed annealed sample
TiN
Ti-O-N bond
Si3N4
Intensity
404
402
400
398
396
394
Binding energy

Fig. 4(c)

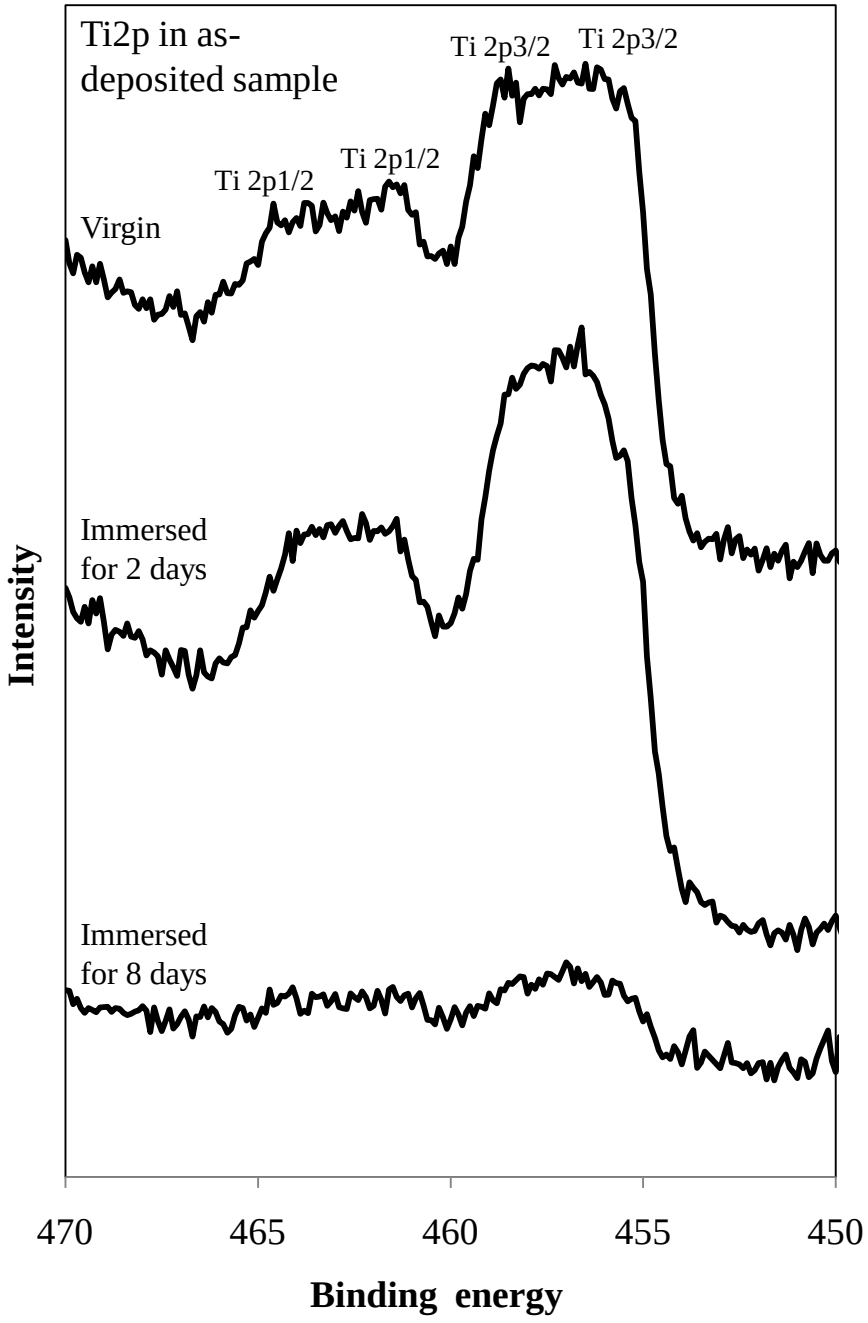
Ti2p in as-deposited sample
Ti 2p3/2
Ti 2p3/2
Ti 2p1/2
Ti 2p1/2
Virgin
Immersed for 2 days
Immersed for 8 days
Intensity
470
465
460
455
450
Binding energy

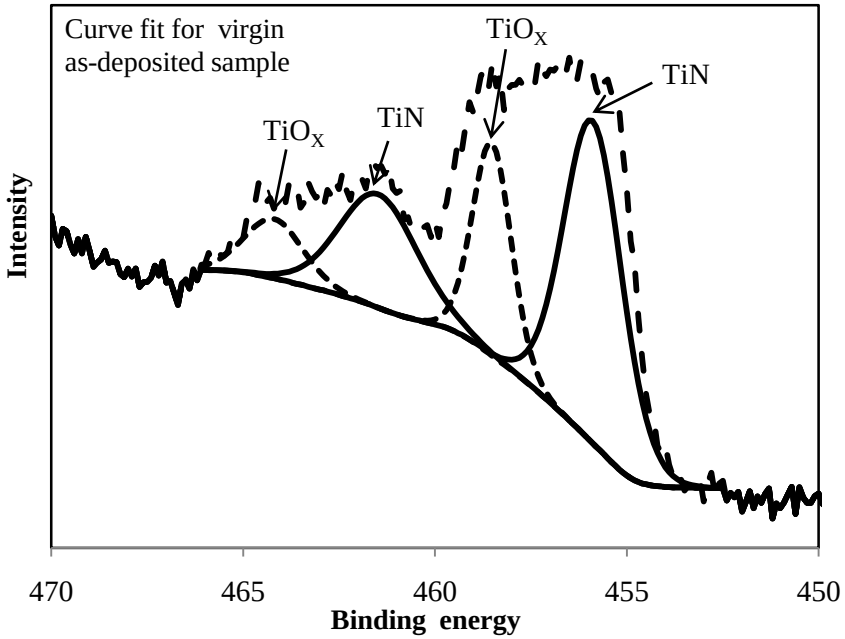
Curve fit for virgin as-deposited sample
TiOX
TiN
TiOX
TiN
Intensity
470
465
460
455
450
Binding energy

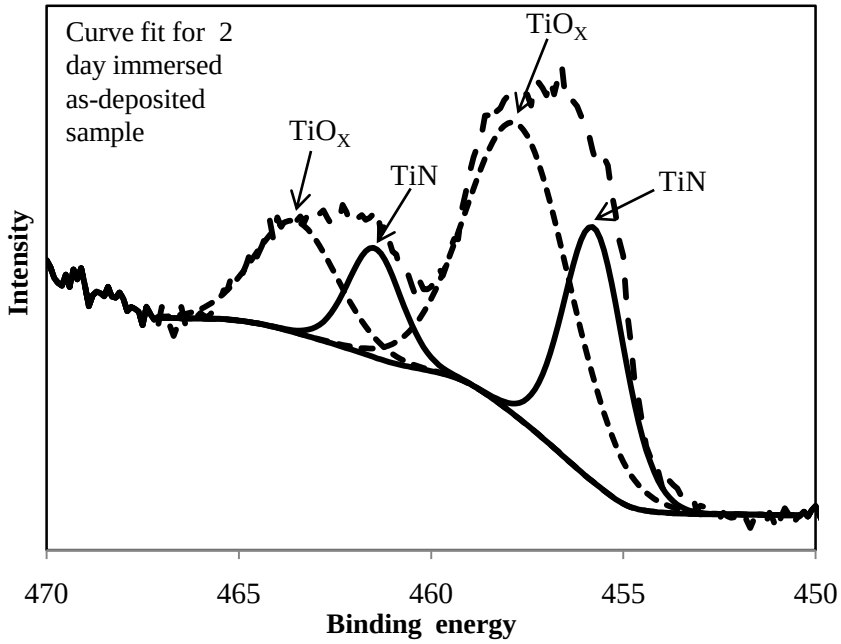
Curve fit for 2 day immersed as-deposited sample
TiOX
TiOX
TiN
TiN
Intensity
470
465
460
455
450
Binding energy

Fig. 4(d)

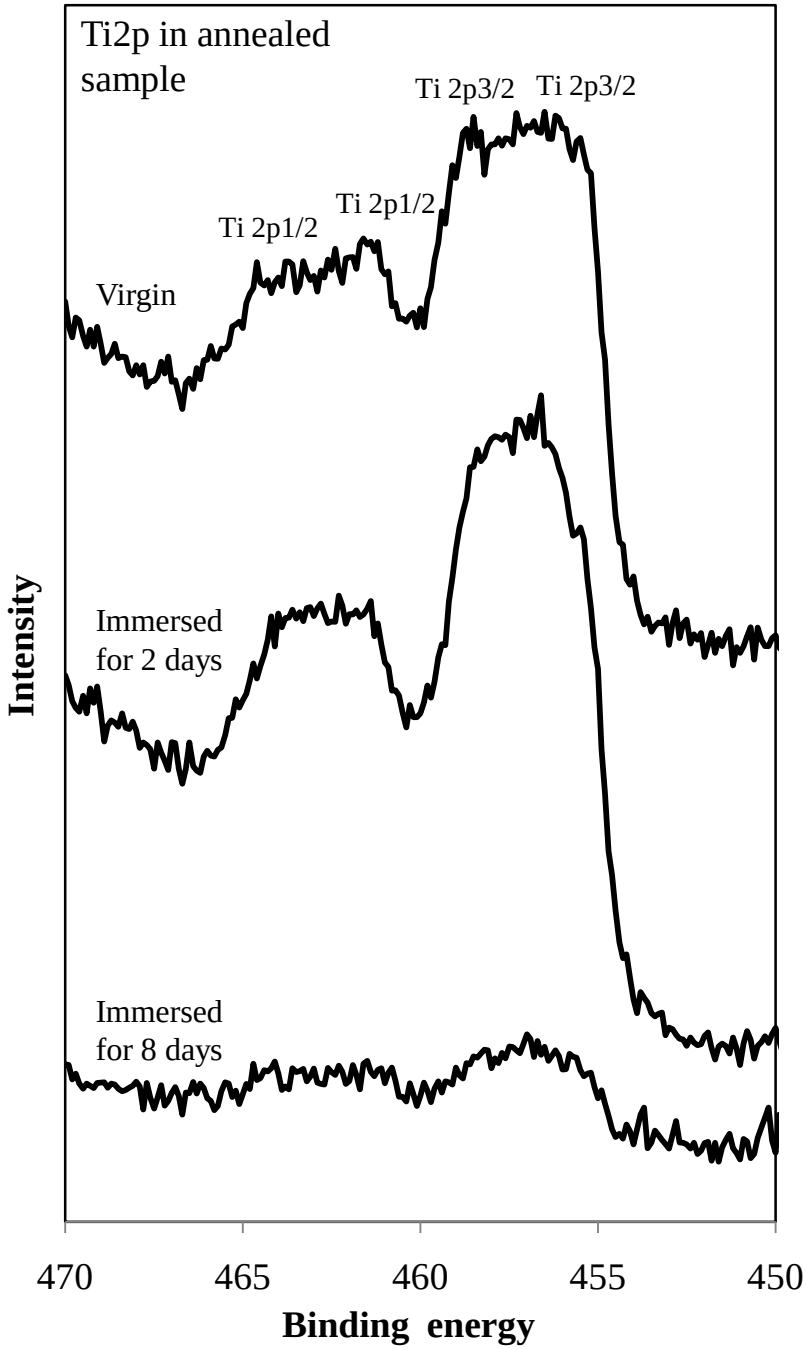
Ti2p in annealed sample
Ti 2p3/2
Ti 2p3/2
Ti 2p1/2
Ti 2p1/2
Virgin
Immersed for 2 days
Immersed for 8 days
Intensity
470
465
460
455
450
Binding energy

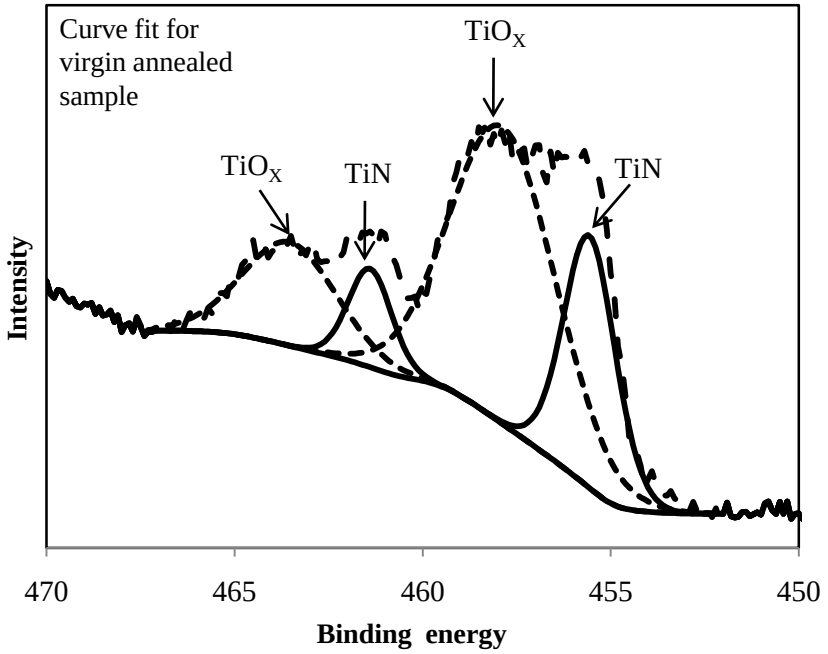
Curve fit for virgin annealed sample
TiOX
TiOX
TiN
TiN
Intensity
470
465
460
455
450
Binding energy

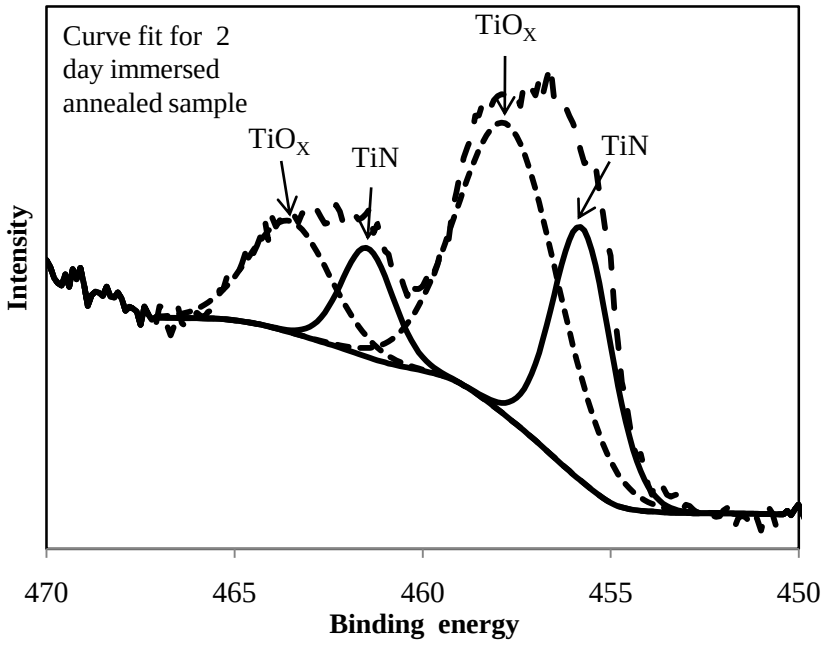
Curve fit for 2 day immersed annealed sample
TiOX
TiOX
TiN
TiN
Intensity
470
465
460
455
450
Binding energy

Fig. 4(e) & (f)

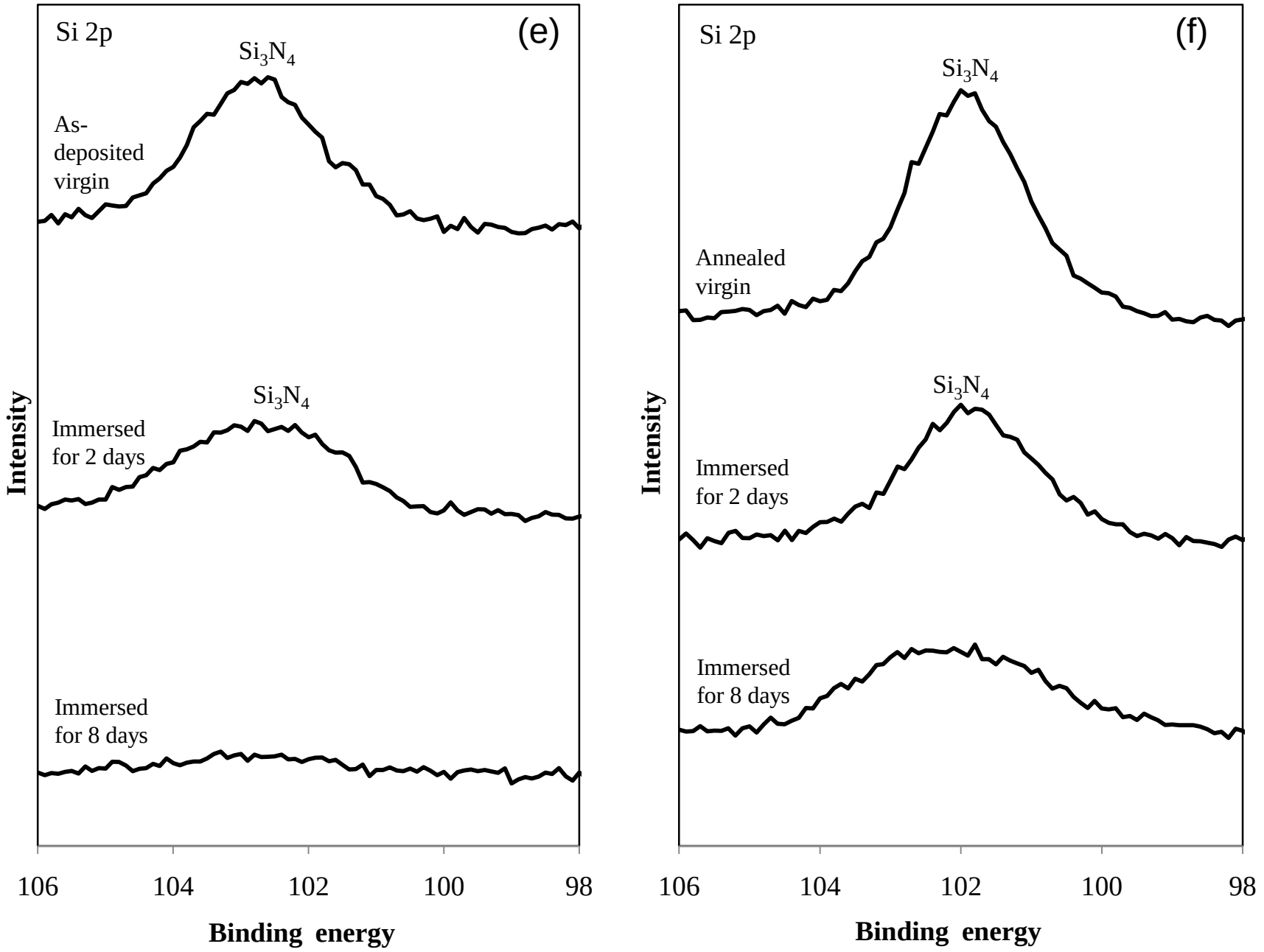
Si 2p
(e)
Si_3N_4
As-deposited virgin
Si_3N_4
Immersed for 2 days
Immersed for 8 days
Intensity
106
104
102
100
98
Binding energy
Si 2p
(f)
Si_3N_4
Annealed virgin
Si_3N_4
Immersed for 2 days
Immersed for 8 days
Intensity
106
104
102
100
98
Binding energy

Fig.5(a)

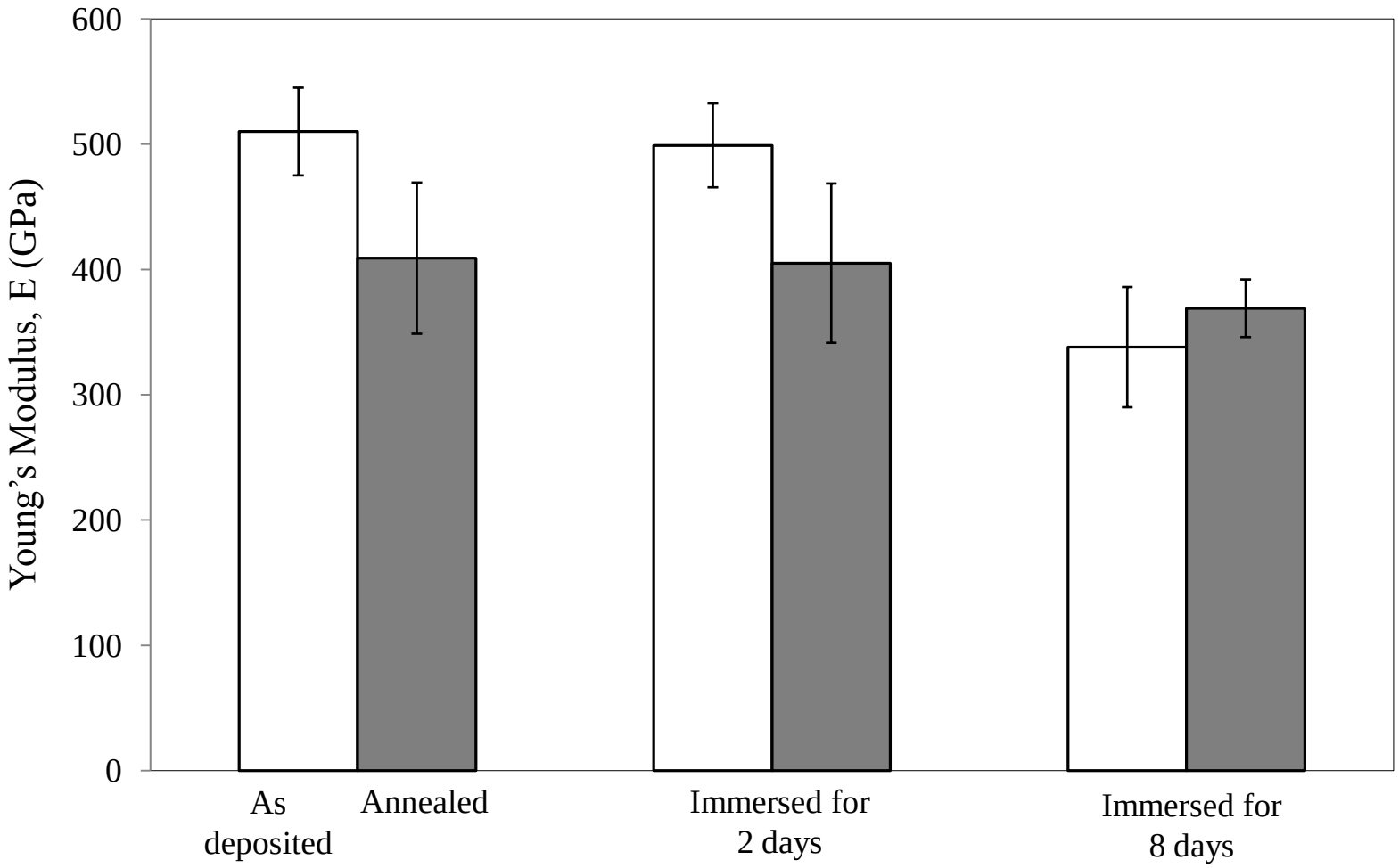
Young's Modulus, E (GPa)
600
500
400
300
200
100
0
As deposited
Annealed
Immersed for 2 days
Immersed for 8 days

Fig.5(b)

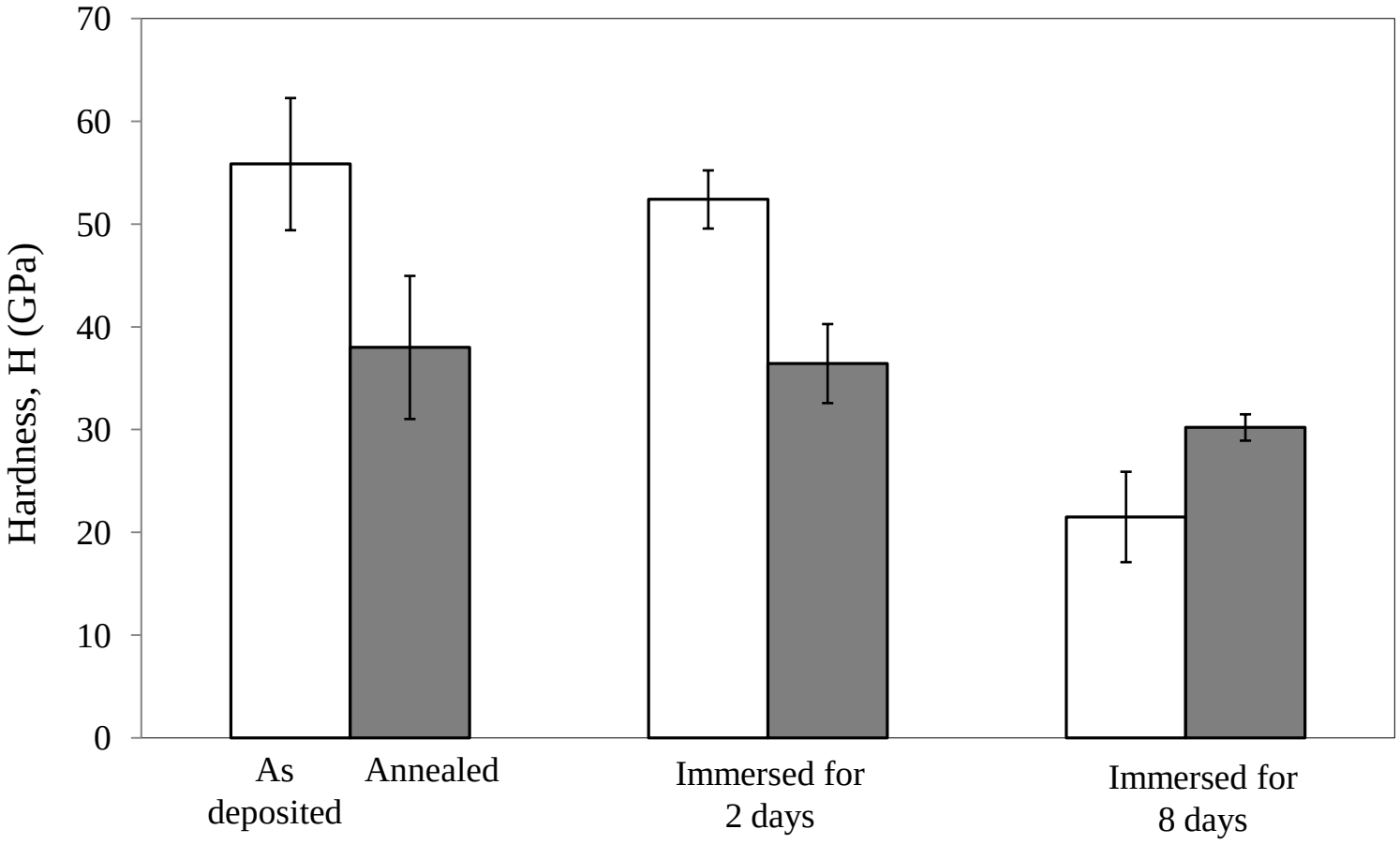
Hardness, H (GPa)
70
60
50
40
30
20
10
0
As deposited
Annealed
Immersed for 2 days
Immersed for 8 days

Fig.6

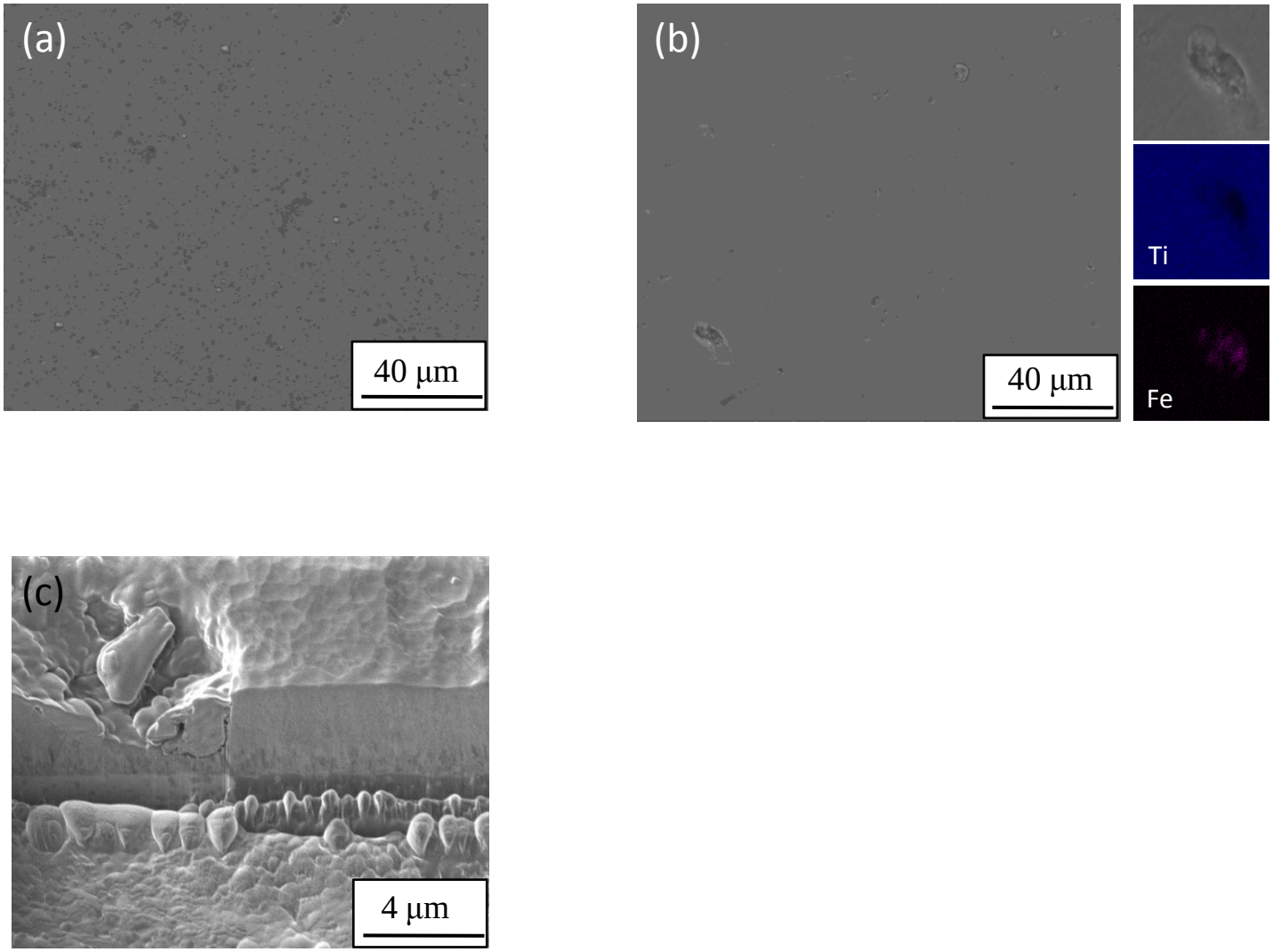

Fig. 7

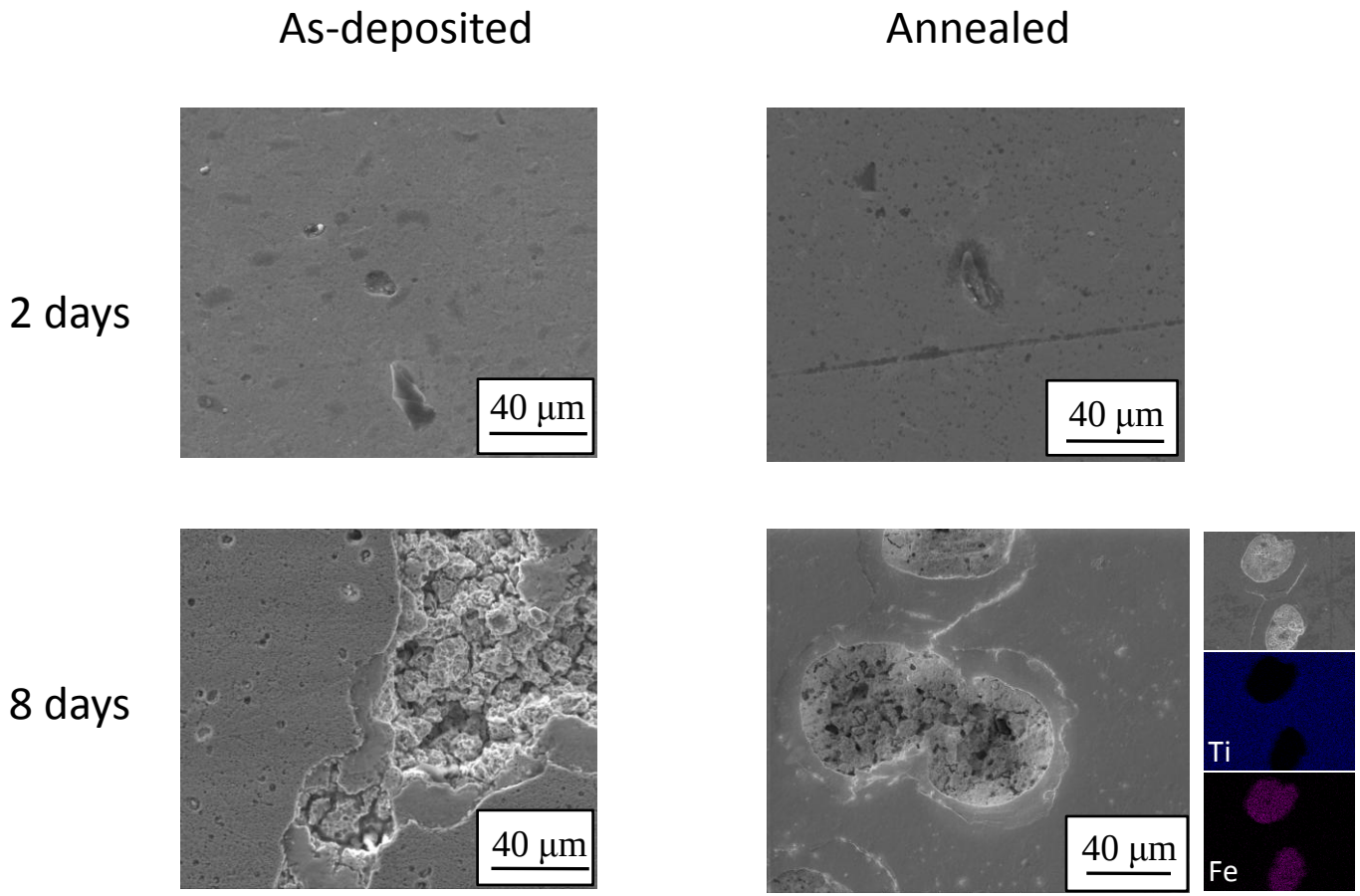

Fig. 8

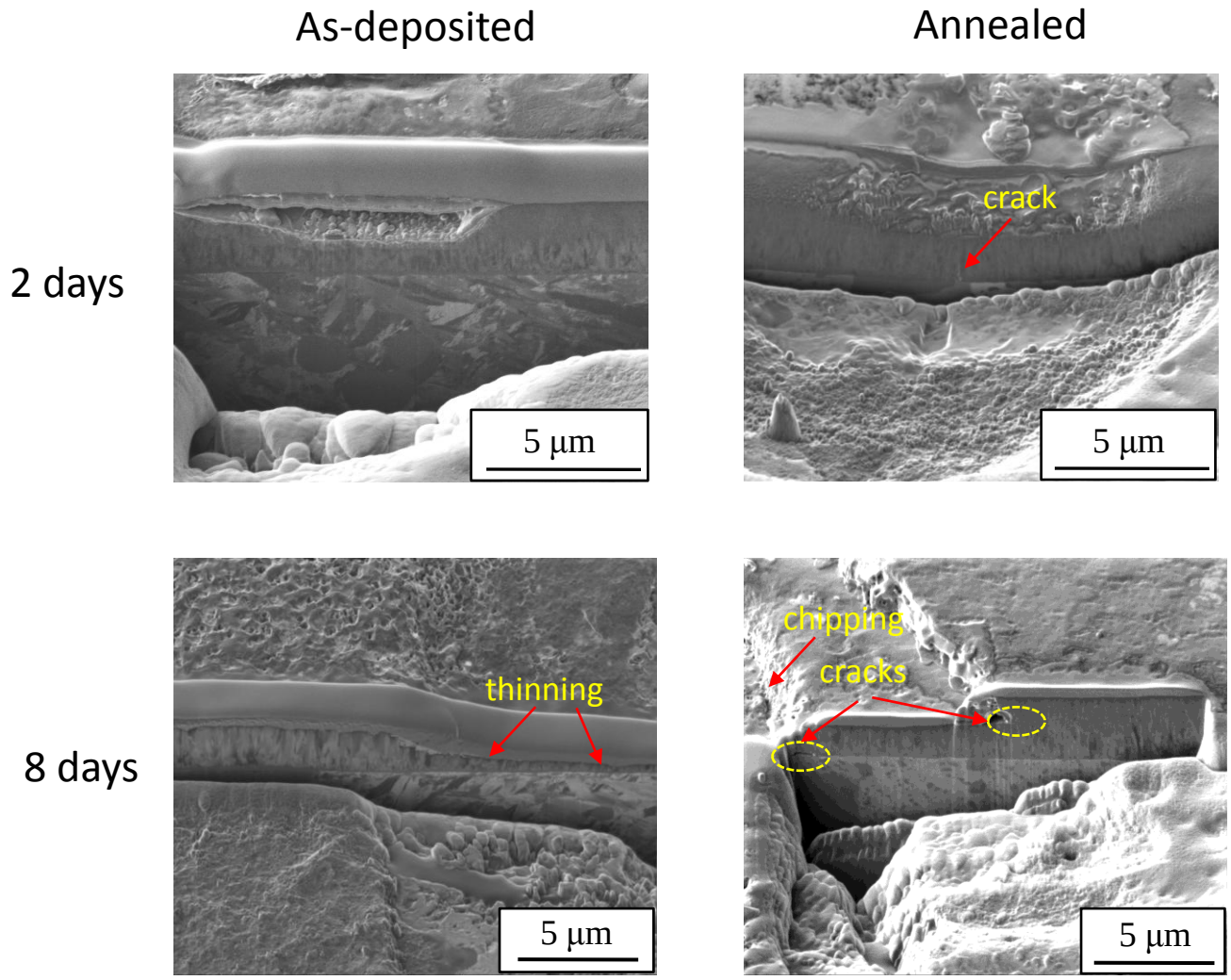
As-deposited
Annealed
2 days
8 days
crack
thinning
chipping
cracks
5 µm
5 µm
5 µm
5 µm

Fig. 9

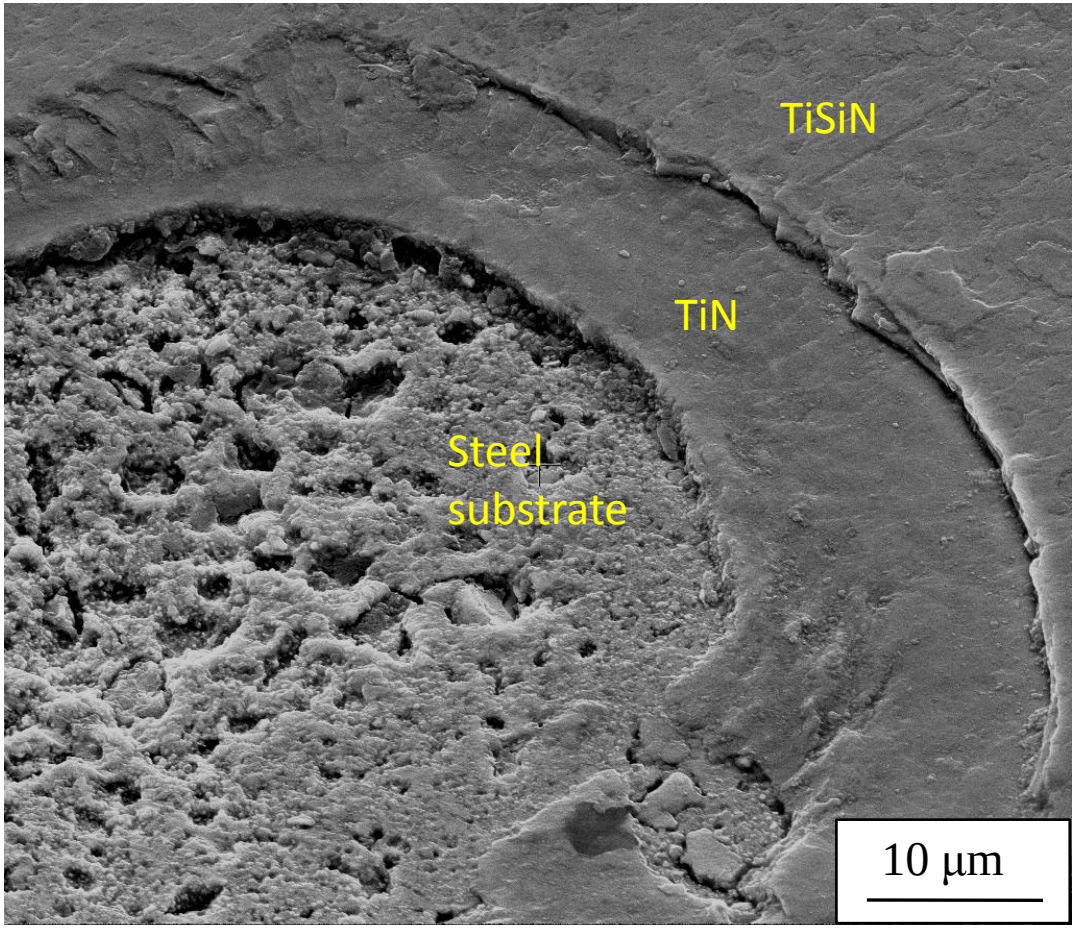

Fig. 10(a)

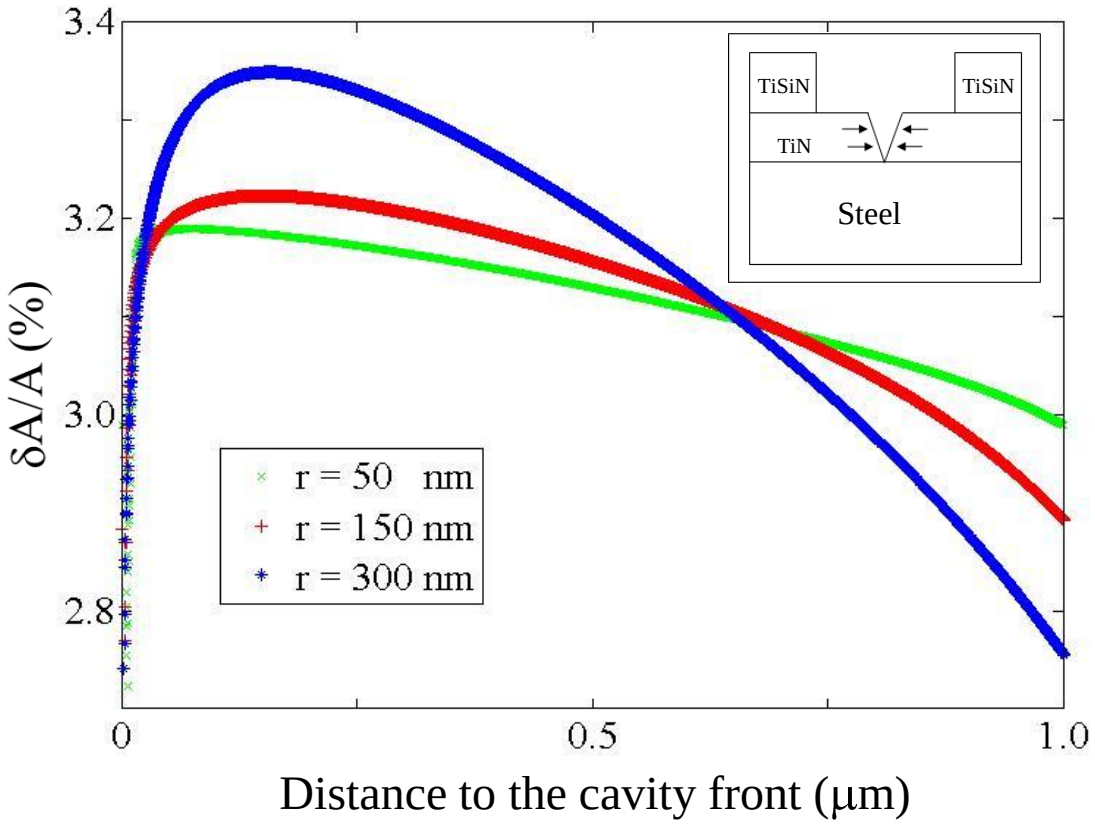
3.4
3.2
3.0
2.8
δA/A (%)
0
0.5
1.0
Distance to the cavity front (μm)
r = 50 nm
r = 150 nm
r = 300 nm
TiSiN
TiSiN
TiN
Steel

Fig. 10(b)

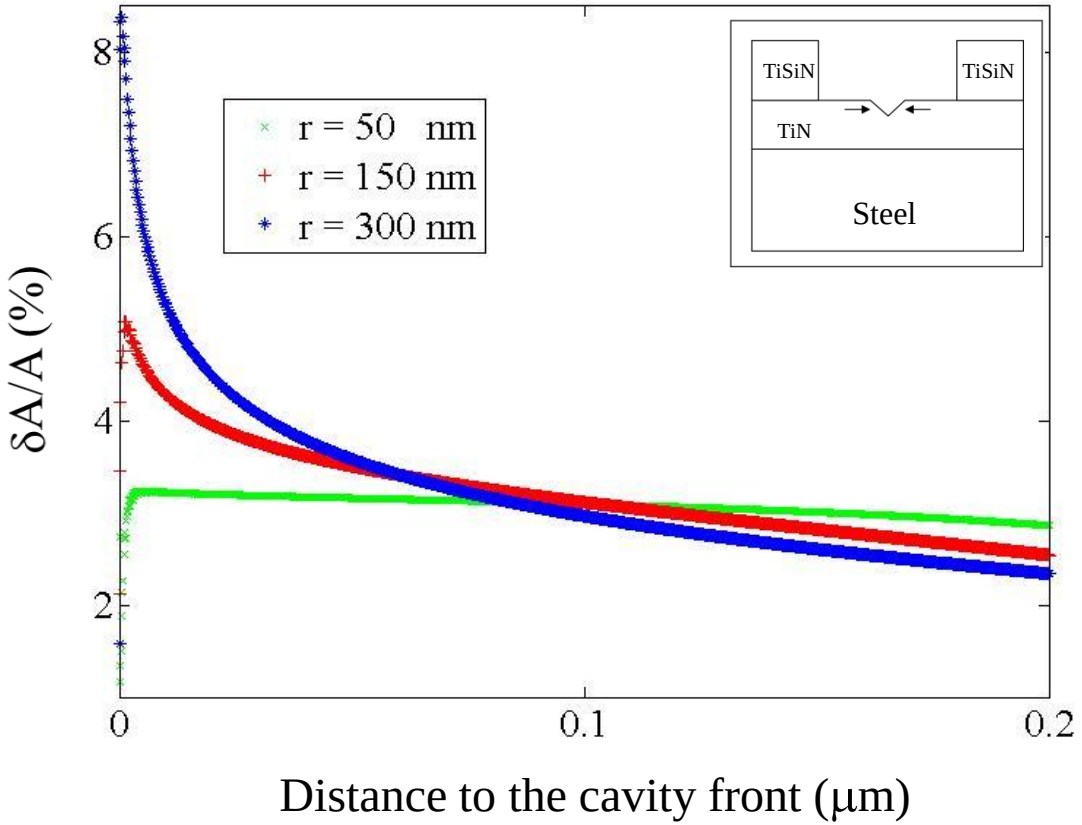
r = 50 nm
r = 150 nm
r = 300 nm
TiSiN
TiSiN
TiN
Steel
δA/A (%)
8
6
4
2
0
0.1
0.2
Distance to the cavity front (μm)